


















Shining a Light on the Connections between Galactic Outflows Seen in Absorption and Emission Lines

XINFENG XU ^{1,2} ALAINA HENRY ^{3,4} TIMOTHY HECKMAN ^{3,5} CODY CARR ^{6,7} ALLISON L. STROM ^{1,2}
TUCKER JONES ⁸ DANIELLE A. BERG ⁹ JOHN CHISHOLM ⁹ DAWN ERB ¹⁰ BETHAN L. JAMES ¹¹
ANNE JASKOT ¹² CRYSTAL L. MARTIN ¹³ MATILDE MINGOZZI ⁴ PETER SENCHYNA ¹⁴ NAMRATA ROY ³
CLAUDIA SCARLATA ¹⁵ AND DANIEL P. STARK ¹⁶

¹*Department of Physics and Astronomy, Northwestern University, 2145 Sheridan Road, Evanston, IL, 60208, USA.*

²*Center for Interdisciplinary Exploration and Research in Astrophysics (CIERA), 1800 Sherman Avenue, Evanston, IL, 60201, USA.*

³*Center for Astrophysical Sciences, Department of Physics & Astronomy, Johns Hopkins University, Baltimore, MD 21218, USA*

⁴*Space Telescope Science Institute, 3700 San Martin Drive, Baltimore, MD 21218, USA*

⁵*School of Earth and Space Exploration, Arizona State University, Tempe, AZ 85287, USA*

⁶*Center for Cosmology and Computational Astrophysics, Institute for Advanced Study in Physics, Zhejiang University, Hangzhou 310058, China*

⁷*Institute of Astronomy, School of Physics, Zhejiang University, Hangzhou 310058, China*

⁸*Department of Physics and Astronomy, University of California Davis, 1 Shields Avenue, Davis, CA 95616, USA*

⁹*Department of Astronomy, The University of Texas at Austin, 2515 Speedway, Stop C1400, Austin, TX 78712, USA*

¹⁰*The Leonard E. Parker Center for Gravitation, Cosmology and Astrophysics, Department of Physics, University of Wisconsin-Milwaukee, 3135 N Maryland Avenue, Milwaukee, WI 53211, USA*

¹¹*AURA for ESA, Space Telescope Science Institute, 3700 San Martin Drive, Baltimore, MD 21218, USA*

¹²*Department of Astronomy, Williams College, Williamstown, MA 01267, United States*

¹³*Department of Physics, University of California, Santa Barbara, Santa Barbara, CA 93106, USA*

¹⁴*The Observatories of the Carnegie Institution for Science, 813 Santa Barbara Street, Pasadena, CA 91101, USA*

¹⁵*Minnesota Institute for Astrophysics, University of Minnesota, 116 Church Street SE, Minneapolis, MN 55455, USA*

¹⁶*Steward Observatory, The University of Arizona, 933 N Cherry Ave, Tucson, AZ, 85721, USA*

(Revised October 1, 2024)

ABSTRACT

Galactic outflows provide important feedback effects to regulate the evolution of the host galaxies. Two primary diagnostics of galactic outflows are broad and/or blueshifted emission and absorption lines. Even though well-established methods exist to analyze these outflow signatures, connections between them are rarely studied and largely unknown. In this paper, we present the first detailed comparisons of the outflow properties measured independently from the two outflow diagnostics for a sample of 33 low-redshift star-forming galaxies. Their UV absorption lines are detected by the Hubble Space Telescope/Cosmic Origin Spectrograph, and optical emission lines are observed by the Keck/Echelle Spectrograph and Imager. We find that several outflow properties derived from emission and absorption lines are tightly correlated. These include outflow maximum velocity, line width, and sizes. Specifically, in a given galaxy, outflows seen in emission lines have smaller maximum velocities, narrower line widths, and smaller sizes than those measured from the absorption lines. These findings can be interpreted by the fact that emission line luminosity is weighted by density squared, while absorption line depth is weighted by density. We then test both spherical and bi-conical outflow models, and find the same outflow velocity and density distributions can explain the observed outflow features in emission and absorption lines for individual galaxies. These results provide novel calibration between galactic outflow properties measured from the two diagnostics and provide valuable insights for future models of galactic outflows by potentially doubling the number of observational constraints.

Keywords: Galactic Winds (572), Galaxy evolution (1052), Galaxy kinematics and dynamics(602), Starburst galaxies (1570), Galaxy spectroscopy (2171)

1. INTRODUCTION

Galactic-scale winds, driven by supernovae ejecta, hot stellar winds, and radiation pressure, have been proposed to explain various feedback effects. These include regulating the star formation (SF) inside the galaxy, enriching the intergalactic and circumgalactic medium with heavy metals, and explaining the “overcooling problem” in cosmological simulations by reducing the baryon fractions in galactic discs (see reviews in, e.g., Naab & Ostriker 2017; Heckman & Best 2023).

Galactic winds have been extensively studied in the low-redshift universe ($z \lesssim 1$, e.g., Heckman et al. 2000; Martin 2005; Rupke & Veilleux 2013; Heckman et al. 2015; Chisholm et al. 2016a,b, 2017; Sugahara et al. 2017; Davis et al. 2023; Guo et al. 2023; Xu et al. 2023a,b; Amorín et al. 2024; Fisher et al. 2024; Reichardt Chu et al. 2024) and are found to be more ubiquitous in galaxies at higher redshift (e.g., Steidel et al. 2010; Newman et al. 2012a,b; Davies et al. 2019; Freeman et al. 2019; Avery et al. 2022; Marasco et al. 2023; Perrotta et al. 2023; Zhang et al. 2024; Kehoe et al. 2024). Two major diagnostics of galactic winds are the blue-shifted absorption lines seen mostly in ultraviolet (UV) spectra and broad emission lines found in the optical and infrared spectra. For both types of spectroscopic features, well-established methods exist for deriving important galactic wind properties. These include the velocity gradient and velocity dispersion of the outflows, how dense the outflows are, and how much mass/energy/momentum is carried out by the outflows (see reviews in, e.g., Veilleux et al. 2020; Thompson & Heckman 2024). Hereafter, we focus on the warm ionized outflows ($T \sim 10,000$ K). For this phase of the gas, the main outflow diagnostics are absorption lines studied in rest-UV, including C II $\lambda 1334$, and Si II multiplet ($\lambda 1190, 1193, 1260, 1304, \text{ and } 1526$), Si III $\lambda 1206$, and Si IV $\lambda \lambda 1393, 1402$, and emission lines studied in rest-optical, including [N II] $\lambda \lambda 6548, 6583$, [O II] $\lambda \lambda 3727, 3729$, [O III] $\lambda \lambda 4959, 5007$, [S II] $\lambda \lambda 6717, 6731$, and the Balmer lines.

Even with the wide number of existing studies, it remains to be seen how the outflow measurements from emission and absorption features are related. Since emission line luminosity are weighted linearly by gas density squared (n^2) and absorption line column density are linearly weighted by n , these two types of outflow measurements should be sensitive to different parts of the outflow. Furthermore, given the fact that

these emission and absorption lines likely trace the same warm-ionized gases in a given galaxy, a unified model (e.g., outflow velocity and density distributions as a function of radius, outflow geometry, etc) may explain both observations from emission and absorption lines.

However, to date, outflows have only been simultaneously studied in absorption and emission in rare, non-representative cases: ULIRGs (Martin 2006) and BALQSOs (Xu et al. 2020), or in single galaxies (e.g., Wood et al. 2015; Martín-Fernández et al. 2016). This problem is mainly due to the difficulty of retrieving a sample of galaxies with both high-quality rest-UV and rest-optical observations. On the one hand, UV bright galaxies cannot have very high column densities of gas, otherwise the dust attenuation would be too significant for us to observe the gas. On the other hand, galaxies have to be at specific redshifts so that their rest-UV bands are bright enough and covered by large ground-based optical telescopes ($1 \lesssim z \lesssim 2$) or UV space telescopes ($z \lesssim 0.4$). This problem persists after the launch of the James Webb Space Telescope (JWST), for which most of the galactic outflow studies are based on emission lines due to the difficulty to detect faint UV continuum in individual galaxies at high redshifts ($3 < z < 9$, e.g., Carniani et al. 2024; Xu et al. 2023c; Zhang et al. 2024). Hence, we have yet to leverage the full suite of observational constraints to yield a consistent picture of outflows and their feedback effects to the hosts.

In this paper, we present this much-needed study, where we assembled a sample of 33 local star-forming (SF) galaxies with high-SNR and moderate-resolution UV+optical spectra. For the first time, we present a systematic joint analysis of the two types of outflow diagnostics. Our sample is focused on compact, low-mass SF galaxies ($< 10^{10} M_{\odot}$), where the majority show clear outflow features and may provide strong feedback to the host galaxies (e.g., Heckman et al. 2015). Similar low-mass galaxies have also been found to host strong outflows at earlier universe ($3 < z < 9$, e.g., Carniani et al. 2024).

The structure of this paper is as follows. In Section 2, we introduce the observations and data reductions. In Section 3, we describe how to extract outflow signatures from rest-UV absorption and rest-optical emission lines, respectively. In Section 4, we compare the outflow properties from absorption and emission lines. Finally, we discuss our findings in Section 5, where we also construct models to explain the discovered correlations be-

tween two outflow diagnostics. We conclude the paper in Section 6.

2. OBSERVATIONS AND DATA REDUCTIONS

2.1. Sample Selection

We construct the sample in two steps. We first identify galaxies that have archival rest-UV spectra from at least one medium resolution grating of the Cosmic Origins Spectrograph (COS) onboard HST, including G130M and G160M. We require the spectra to cover at least the Si II or Si IV absorption lines for outflow diagnostics. Then we cross-match the galaxies with the Keck and Very Large Telescope (VLT) archives to search for high-quality optical observations (spectral resolution $\gtrsim 4000$, $H\alpha$ peak SNR > 100). Finally, we gather a joint sample of 33 low-redshift SF galaxies with redshifts between 0.002 – 0.27. Our galaxies cover a wide range of stellar mass [$\log (M_*/M_\odot) \sim 5 - 10$, Section 3.1], star formation rate [$\log \text{SFR} / (M_\odot \text{yr}^{-1}) \sim -3$ to $+2$, Section 3.4], and oxygen abundances ($12 + \log(\text{O}/\text{H}) \sim 7.4 - 8.5$). Thus, our galaxies are representative of a large population of local SF galaxies. As shown below, our sample is mainly composed of objects such as Green Peas and extreme emission line galaxies that are analogs to high-redshift objects.

In Figure 1, we show the parameter space (SFR vs M_* relationship, i.e., SFMR) spanned by galaxies in our sample. The details of these measurements are discussed in Section 3. The galaxies with (without) detected outflow features are drawn as filled (hollow) symbols. The linear fit to all galaxies is shown as the orange dashed line. For a comparison, we also present SFMR from other surveys, including 1) the $z \sim 0$ sample from 10^6 SDSS+WISE galaxies published in Chang et al. (2015) as the blue dashed line; 2) the $0.5 < z < 2.5$ samples from Whitaker et al. (2014) that contain $\sim 4 \times 10^4$ SF galaxies in the CANDELS fields as the pink lines; and 3) a comprehensive, high-quality UV catalog built from the COS Legacy Archive Spectroscopic Survey (CLASSY, Berg et al. 2022; James et al. 2022) in the purple solid line. The scatter in all the correlations is $\sim 0.3 - 0.4$ dex.

In general, our galaxies follow the CLASSY SFMR trend. This is as expected since CLASSY is the most complete UV catalog of low-redshift SF galaxies, and 7 out of 33 of our galaxies are included in CLASSY. Besides that, our galaxies (along with CLASSY) are both selected to have UV bright galaxies and have higher SFR than the extrapolated local SFMR trend from SDSS but are close to the $z \sim 1 - 2.5$ galaxies in pink from Whitaker et al. (2014). This suggests that our galax-

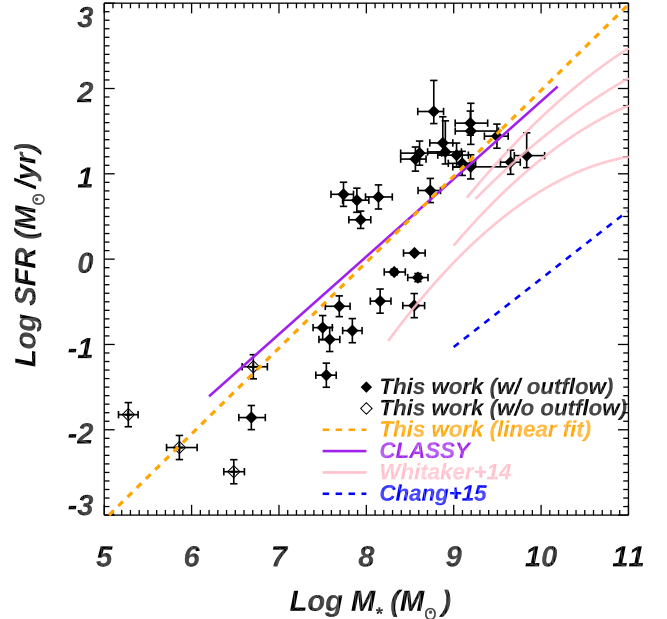


Figure 1. Star formation rate vs stellar mass relationship (SFMR) for galaxies in our sample. Our galaxies with and without detected outflows are drawn as filled and hollow diamonds, respectively. The 1σ errorbars are drawn as crosses around the symbols. The best linear fits to all of our galaxies are shown as the orange dashed line. For comparisons, we present the SFMR trends from $z \sim 0$ SDSS+WISE sample from Chang et al. (2015) as the blue dashed line, $z \sim 1 - 2.5$ SF galaxy sample from Whitaker et al. (2014) as the pink lines, and the UV catalog of local SF galaxies from CLASSY survey in purple (Berg et al. 2022; James et al. 2022). Galaxies in our sample mostly represent low-mass SF galaxies and their SFRs are offset to match better with galaxies at cosmic noon instead of with the large populations at $z \sim 0$.

ies have higher star formation that are more commonly seen for galaxies around cosmic noon.

2.2. UV Observations

The UV spectra of galaxies in our sample were gathered from various HST programs. The original programs have diverse goals but most of the galaxies are selected to be SF galaxies and are analogs to high-redshift ones. These programs include studies of outflows and starbursts in Green Pea galaxies (PI-Henry: 12928; PI-Jaskot: 13293, 14080), studies of local Lyman Break Galaxies (PI-Heckman: 11727, 13017); analyses of extreme emission line galaxies (PI-Stark: 14168, 14679, 15185, 15646; PI-Senchyna: 17526), studies of galactic outflows in SF galaxies (PI-Chisholm: 15099), studies of Lyman continuum and $\text{Ly}\alpha$ in local SF galaxies (PI-Jaskot: 15626; PI-Gazagnes: 16643); and Far-UV catalog of nearby SF galaxies (PI-Berg: 15840). We download their reduced 1D spectra and COS acquisi-

tion images from the HST Mikulski Archive for Space Telescopes (MAST) for later analyses. The COS spectra for each galaxy are coadded and binned to be $R \sim 9000$ (FWHM $\sim 33 \text{ km s}^{-1}$). The typical SNR of the UV continuum is from 5 to 10. The information for these observations and their corresponding references are summarized in Table 1.

2.3. Optical Observations and Reductions

Most of our galaxies (29/33) were observed by the Echellette Spectrograph and Imager (ESI) at the Cassegrain focus of the Keck II telescope (Sheinin et al. 2002). ESI covers a broad bandpass (3900 – 11,000Å) with a single exposure. The observations were done from 2016 to 2017 in several programs (PIs: Henry and Jones), given slit sizes from $0''.75$ to $1''$. These sizes are similar to the $\sim 0''.8 - 1''$ diameters that are less affected by vignetting in the HST/COS aperture. Given the slit sizes, the data have a spectral resolution of $\sim 56 - 75 \text{ km s}^{-1}$ (FWHM). The seeing is typically $\sim 0''.7$. The detailed exposure times are shown in Table 1.

We reduce the data following the *ESIRedux* pipeline¹ with several custom steps. First, we turn off the default removal of cosmic rays in the pipeline and do manual checks instead. This is because the default pipelines incorrectly identify and mask out the strong emission lines (e.g., [O III] 5007 and $H\alpha$) from our galaxies. We also find the sky was commonly over-subtracted around strong emission lines, especially when the lines are spatially extended. Thus, we add another input parameter to manually define the sky regions, which are measured from the 2D spectra around the strong lines for each galaxy. Finally, we note that in the co-added spectra, the adjacent diffraction orders in Echelle spectra can exhibit semi-sinusoidal features where the orders are stitched together. Thus, for each galaxy, we apply another flux calibration for these features. We conduct spline fits to the galaxy’s continuum spectra from ESI and Sloan Digital Sky Survey (SDSS), separately. Then we scale the ESI spectrum by matching its spline fit to the SDSS one of the same galaxy. We have checked that this only has minor effects on our measurements of emission lines since they are scaled together with the local continuum levels.

We also include four galaxies observed by the X-Shooter spectrograph (Vernet et al. 2011) mounted on the VLT as part of the ESO program ID 085.B-0784(A) and 096.B-0192(A) (PI: Overzier, Loaiza-Agudelo et al. 2020). These observations were done in slit mode ($11''$

long slit) to obtain simultaneous spectra from the three arms, i.e., UVB ($1''$ wide slit, $R \sim 5100$), VIS ($0''.9$ wide slit, $R \sim 8800$), and NIR ($0''.9$, $R \sim 5100$). Our main emission line ($H\alpha$) fall into the VIS bands, which yield a resolution with FWHM $\sim 34 \text{ km s}^{-1}$, which is similar to our ESI data. The X-Shooter exposure times are also listed in Table 1. The detailed data reduction is done with ESO/X-Shooter pipeline (Modigliani et al. 2010) and the EsoRex command-line recipes and is discussed in Loaiza-Agudelo et al. (2020).

3. UV AND OPTICAL MEASUREMENTS

3.1. Spectral Energy Distribution Fitting

To constrain the continuum level and remove the starlight contribution, we conduct SED fitting of our UV and optical spectra, separately. For the UV, we adopt the *FICUS* code² to fit the coadded HST/COS data for each galaxy. Detailed descriptions of the methods can be found in Chisholm et al. (2019); Saldana-Lopez et al. (2022). For a brief summary, we fit each observed spectrum with a linear combination of multiple bursts of single-metallicity and single-age stellar population models from Starburst99 (Leitherer et al. 1999, 2010). A nebular continuum was also included by self-consistently processing the stellar population synthesis models through the cloudy v17.0 code (Ferland et al. 2017). We assume attenuation law from Reddy et al. (2016). In addition to the continuum level, we also get various important parameters from the fitting, including the galaxy’s light-weighted metallicity, stellar wind absorption, and stellar ages and dust extinction.

For the optical spectra, we conduct SED fitting using the *Prospector* code (Johnson et al. 2021). We follow the approaches in Xu et al. (2022a) and assume a non-parametric star formation history (SFH) with a Kroupa IMF (Kroupa 2001) and the attenuation law from Reddy et al. (2015). We adopt the isochrone library of MIST (Choi et al. 2016), spectral library of C3K (Conroy et al. 2019), and dust emission model from Draine & Li (2007). We also get the stellar mass of galaxies from the best SED fits (listed in Table 3).

Before the SED fitting, we masked out spectral regions $\pm 550 \text{ km s}^{-1}$ around ISM absorption lines, nebular emission lines, Milky Way (MW) absorption lines, and Geocoronal emission lines. For especially broad lines, including $Ly\alpha$, $[H\alpha]$, [O III] $\lambda 5007$, we increase the mask region to $\pm 1500 \text{ km s}^{-1}$. Finally, for each galaxy, we normalize the spectra based on its best-fit SEDs.

¹ <https://www2.keck.hawaii.edu/inst/esi/ESIRedux/index.html>

² <https://github.com/asalda/FiCUS>

Table 1. UV and Optical Observations for Galaxies in Our Sample

ID	RA	Dec	z^1	T(G130M) ²	T(G160M) ²	Ref. ³	T(OPT) ²	OPT Instrument
				(s)	(s)		(s)	
J0055-0021	00:55:27	-00:21:48	0.1672	5040	2970	(a)	2560	VLT/X-Shooter
J0150+1308	01:50:28	+13:08:58	0.1464	1327	1623	(a)	2560	VLT/X-Shooter
J0808+1728	08:08:41	+17:28:56	0.0442	4451	4451	(b)	3600	Keck/ESI
J0815+2156	08:15:52	+21:56:24	0.1409	0	6809	(c)	3600	Keck/ESI
J0851+5840	08:51:16	+58:40:55	0.0919	12318	0	(b)	3300	Keck/ESI
J0911+1831	09:11:13	+18:31:08	0.2622	2073	6530	(d, e)	1200	Keck/ESI
J0926+4427	09:26:00	+44:27:37	0.1807	5640	6180	(a, f)	1500	Keck/ESI
J0942+0928	09:42:56	+09:28:16	0.0109	0	2608	(g)	4800	Keck/ESI
J0942+3547	09:42:52	+35:47:26	0.0149	10754	2664	(g, h)	8100	Keck/ESI
J0944-0038	09:44:01	-00:38:31	0.0049	6086	34582	(f, g)	7200	Keck/ESI
J1024+0524	10:24:29	+05:24:50	0.0332	4296	2608	(f, g)	9000	Keck/ESI
J1044+0353	10:44:57	+03:53:13	0.0126	6853	34871	(f, i)	2560	VLT/X-Shooter
J1053+5237	10:53:31	+52:37:53	0.2526	824	2736	(d, e)	1200	Keck/ESI
J1129+2034	11:29:14	+20:34:52	0.0047	6885	2588	(f, g)	5400	Keck/ESI
J1133+6513	11:33:04	+65:13:41	0.2414	1232	4588	(d, e)	3900	Keck/ESI
J1137+3524	11:37:22	+35:24:27	0.1944	1264	2339	(e)	1200	Keck/ESI
J1148+2546	11:48:27	+25:46:10	0.0451	4552	2624	(f, g)	9000	Keck/ESI
J1155+5739	11:55:28	+57:39:52	0.0172	0	2852	(g)	9000	Keck/ESI
J1200+2719	12:00:16	+27:19:59	0.0819	4610	0	(b)	3300	Keck/ESI
J1215+2038	12:15:18	+20:38:25	0.0027	0	2616	(g)	5400	Keck/ESI
J1219+1526	12:19:04	+15:26:09	0.1956	716	2303	(e)	2100	Keck/ESI
J1222+0434	12:22:25	+04:34:04	0.0043	0	2604	(g)	4200	Keck/ESI
J1226+0415	12:26:12	+04:15:36	0.0942	11568	0	(b)	2700	Keck/ESI
J1230+1202	12:30:48	+12:02:43	0.0042	0	2612	(g)	7200	Keck/ESI
J1244+0215	12:44:23	+02:15:40	0.2394	2042	6507	(e)	2100	Keck/ESI
J1248+1234	12:48:35	+12:34:03	0.2634	1644	6372	(e)	4200	Keck/ESI
J1311-0038	13:11:31	-00:38:44	0.0811	8426	0	(b)	3600	Keck/ESI
J1416+1223	14:16:12	+12:23:40	0.1228	2379	4636	(j)	2560	VLT/X-Shooter
J1424+4216	14:24:06	+42:16:46	0.1848	1208	0	(e)	1500	Keck/ESI
J1448-0110	14:48:05	-01:10:58	0.0274	9610	5192	(b, f, g)	1200	Keck/ESI
J1457+2232	14:57:35	+22:32:02	0.1486	0	7029	(c)	3300	Keck/ESI
J1509+3731	15:09:34	+37:31:46	0.0326	8095	7550	(b)	3600	Keck/ESI
J1735+5703	17:35:01	+57:03:09	0.0472	5519	0	(b)	900	Keck/ESI

Note. –

- (1) Redshift of the objects matched to the peak of the fitted narrow component of Balmer emission lines.
- (2) Exposure times in seconds analyzed for each galaxy with COS G130M, COS G160M, and the optical instrument, respectively. Zero means no observations exist with that instrument by the time we did the analyses.
- (3) HST programs and the main references for each object: (a): HST-GO-11727, PI: Heckman (Heckman et al. 2015); (b): HST-GO-14080, PI: Jaskot (Jaskot et al. 2017); (c): HST-GO-13293, PI: Jaskot (Jaskot & Oey 2014); (d): HST-GO-15626, PI: Jaskot (Flury et al. 2022a,b); (e): HST-GO-12928, PI: Henry (Henry et al. 2015); (f): HST-GO-15840, PI: Berg (Berg et al. 2022; James et al. 2022); (g): HST-GO-14168, PI: Stark (Senchyna et al. 2017); (h): HST-GO-15099, PI: Chisholm (Chisholm et al. 2019); (i): HST-GO-15646, PI: Stark (Senchyna et al. 2022); (j): HST-GO-13017, PI: Heckman (Heckman et al. 2015); (g): HST-GO-15185, PI: Stark (Senchyna et al. 2021).

3.2. Spectral Line Fitting

In the UV spectra of SF galaxies, outflow features appear as broad and blueshifted absorption lines (e.g., Heckman et al. 2015). Similarly, outflows can show as broad emission lines in optical spectra³ (e.g., Freeman et al. 2019). To compare the possible outflow signatures from UV and optical spectra, we need to first isolate them from the static interstellar medium (ISM) that is not moving out of the galaxy. To do so, we fit the diagnostic absorption and emission lines with multiple Gaussian profiles. In the following sections, we explain our line fitting techniques for UV and optical, separately. For each galaxy, we adopt the same redshift for its UV and optical lines, which is constrained by the peak of the narrow emission component.

3.2.1. Fitting UV Absorption Lines

For diagnostic UV absorption lines, we follow the same methodology described in Xu et al. (2022b) to fit them. These lines include C II $\lambda 1334$, the Si II multiplet ($\lambda 1190$, 1193, 1260, 1304, and 1526), Si III $\lambda 1206$, and Si IV $\lambda \lambda 1393$, 1402, whenever they are cleanly detected. For a summary, we fit each UV absorption trough using a double-Gaussian profile, separately. This includes a narrow Gaussian with its center fixed at zero velocity representing the static ISM and a broad, blueshifted Gaussian for the outflow component. We also attempted to fit the absorption trough using a single-Gaussian profile centered at zero velocity. We then compare the fitting results of single- and double-Gaussian profiles and apply an F-test to determine if the fitted absorption trough requires the additional broad component, i.e., if the trough contains outflow signatures (see Equation (1) in Xu et al. 2022b). We run F-test with $\alpha = 0.05$, i.e., at 95% confidence level. Examples of the fits are shown in Figure 2, while the fits for all galaxies are presented in Appendix A. We find most of our galaxies (27/33) exhibit outflow signatures in the UV absorption lines.

3.2.2. Fitting Optical Emission Lines

For emission lines in the optical spectra, outflow features can exhibit as broad wings and we fit them following the strategies above with modifications taken from Newman et al. (2012b); Freeman et al. (2019) (hereafter referred to as N12 and F19). The major diagnostic emission lines include [O II] $\lambda \lambda 3726$, 3729, [O III] $\lambda 4363$, [O III] $\lambda \lambda 4959$, 5007, [N II] $\lambda \lambda 6549$, 6585, [S II] $\lambda \lambda 6717$, 6731 and the Balmer lines ($H\alpha$, $H\beta$, and $H\gamma$).

³ While Active Galactic Nucleus (AGN) activities can also generate the broad emission lines, for the SF galaxies in our sample, we didn't detect clear AGN features.

Given the high SNR of our optical spectra, we do not tie the kinematics [i.e., velocity centers (v_c) and widths (FWHM)] for all emission lines in one galaxy. But we do tie the parameters for lines that are constrained by atomic physics. This includes Balmer lines that share the same kinematics for the broad component (or the narrow component). Thus, we have two free parameters for each Balmer line, i.e., broad amplitude (A_b), and narrow amplitude (A_n), while there are four shared parameters over all Balmer lines, i.e., $v_{c,b}$, $v_{c,n}$, $FWHM_b$, and $FWHM_n$. Hereafter, b and n stand for broad and narrow components, respectively. A similar case applies to the [S II] $\lambda \lambda 6717$, 6731 doublet. For [O III] $\lambda \lambda 4959$, 5007 or [N II] $\lambda \lambda 6549$, 6585 doublets, they share the same $v_{c,b}$, $v_{c,n}$, $FWHM_b$, and $FWHM_n$, while their doublet line ratios are also constrained by the atomic physics (2.98 and 2.93, respectively, Osterbrock & Ferland 2006). Examples of the fits are shown in the bottom panels of Figure 2.

We have checked that the final fitted $FWHM_b$ (or $FWHM_n$) for different lines are similar within error bars even though we do not fit them simultaneously. For lines that are blended or weak, e.g., [O II] $\lambda \lambda 3726$, 3729 and [O III] $\lambda 4363$, the broad and narrow components cannot be reliably distinguished. Thus, their line kinematics are tied to the ones from [O III] $\lambda \lambda 4959$, 5007 doublet.

For around two-thirds of our galaxies, we find the double-Gaussian profile described above is sufficient to fit the optical emission lines well. However, this method fails in the other galaxies, where the emission lines are commonly asymmetric. For these galaxies, we add an additional narrow Gaussian component, which stands for the ISM gas in kinematically different H II regions from the main ISM component. We have also adopted an F-test to determine if this additional Gaussian is necessary in such cases.

3.2.3. Line Fitting Results

We present the line fitting results for all of our galaxies in Appendix A. In each figure, the top two rows are for absorption lines in the UV, while the bottom two rows are for the optical emission lines of the same galaxy for a comparison. Data and uncertainties are shown as black and gray histograms. The best-fitted static ISM and outflow components are shown in green and blue lines. The additional narrow component is shown in orange lines when needed, and the sum of all models is shown in red lines. We also add the insets to show a zoom-in view of the extended emission-line wings.

At the first glance, by comparing the outflow components (in blue) of emission and absorption lines for each galaxy, the data strongly suggest that outflow sig-

Table 2. Measured Properties from the Absorption and Emission Lines⁽¹⁾

ID	Absorption Lines			Emission Lines		
	Param.	v_{95}^{out}	FWHM^{out}	$\log(n_e)$	$v_{95, \text{H}\alpha}^{\text{out}}$	$\text{HWHM}_{\text{H}\alpha}^{\text{out}}$
Unit	(km s ⁻¹)	(km s ⁻¹)	log(cm ⁻³)	(km s ⁻¹)	(km s ⁻¹)	log(cm ⁻³)
J0055-0021	-412 ⁺⁵¹ ₋₅₁	591 ⁺¹⁰⁸ ₋₁₀₈	1.0 ^{+0.4} _{-0.4}	-330 ⁺¹² ₋₁₂	212 ⁺¹ ₋₁	2.5 ^{+0.06} _{-0.07}
J0150+1308	-390 ⁺¹⁶ ₋₁₆	345 ⁺⁶³ ₋₆₃	0.6 ^{+0.4} _{-0.4}	-204 ⁺¹² ₋₁₂	132 ^{+0.1} _{-0.1}	2.6 ^{+0.03} _{-0.03}
J0808+1728	No Outflow	-124 ⁺⁵ ₋₅	63 ^{+0.1} _{-0.1}	...
J0815+2156	-401 ⁺²⁰¹ ₋₂₀₁	328 ⁺²⁴⁶ ₋₂₄₆	1.5 ^{+0.3} _{-0.3}	-171 ⁺⁷ ₋₇	93 ⁺³ ₋₃	...
J0851+5840	-216 ⁺⁹⁰ ₋₉₀	280 ⁺¹⁰⁴ ₋₁₀₄	0.7 ^{+0.3} _{-0.3}	-142 ⁺⁸⁽²⁾ ₋₈	75 ⁺³ ₋₃	...
J0911+1831	-431 ⁺⁵⁹ ₋₅₉	497 ⁺¹³³ ₋₁₃₃	1.1 ^{+0.4} _{-0.4}	-336 ⁺⁹ ₋₉	215 ⁺⁸ ₋₈	...
J0926+4427	-445 ⁺⁹ ₋₉	402 ⁺¹³⁰ ₋₁₃₀	1.0 ^{+0.4} _{-0.4}	-327 ⁺⁷ ₋₇	190 ⁺³ ₋₃	2.0 ^{+0.05} _{-0.05}
J0942+3547	-280 ⁺⁷⁶ ₋₇₆	318 ⁺⁶⁸ ₋₆₈	0.4 ^{+0.2} _{-0.2}	-128 ⁺⁵ ₋₅	75 ^{+0.1} _{-0.1}	...
J0942+0928	-203 ⁺²² ₋₂₂	207 ⁺²³ ₋₂₃	< 0.3	-126 ⁺⁵ ₋₅	60 ^{+0.1} _{-0.1}	2.3 ^{+0.06} _{-0.06}
J0944-0038	-119 ⁺²⁸ ₋₂₈	163 ⁺⁵⁴ ₋₅₄	< 0.4	-157 ⁺⁵ ₋₅	85 ⁺² ₋₂	...
J1024+0524	-249 ⁺³⁶ ₋₃₆	286 ⁺⁵⁴ ₋₅₄	0.5 ^{+0.2} _{-0.2}	-157 ⁺⁵ ₋₅	77 ^{+0.1} _{-0.1}	1.6 ^{+0.05} _{-0.05}
J1044+0353	-143 ⁺²⁰ ₋₂₀	123 ⁺²⁴ ₋₂₄	0.3 ^{+0.2} _{-0.2}	-105 ⁺¹⁴ ₋₁₄	50 ^{+0.1} _{-0.1}	...
J1053+5237	-405 ⁺³⁵ ₋₃₅	413 ⁺¹⁷¹ ₋₁₇₁	1.1 ^{+0.4} _{-0.4}	-331 ⁺⁷ ₋₇	206 ⁺⁵ ₋₅	2.0 ^{+0.05} _{-0.05}
J1129+2034	No Outflow	No Outflow
J1133+6513	-453 ⁺⁵⁰ ₋₅₀	444 ⁺⁴⁹ ₋₄₉	0.7 ^{+0.5} _{-0.5}	-206 ⁺⁷ ₋₇	117 ⁺³ ₋₃	...
J1137+3524	-317 ⁺³⁷ ₋₃₇	334 ⁺⁴⁶ ₋₄₆	1.1 ^{+0.4} _{-0.4}	-330 ⁺⁷ ₋₇	199 ⁺³ ₋₃	1.9 ^{+0.05} _{-0.05}
J1148+2546	-202 ⁺³³ ₋₃₃	239 ⁺⁵² ₋₅₂	< 0.5	-168 ⁺⁵ ₋₅	87 ^{+0.1} _{-0.1}	2.6 ^{+0.006} _{-0.006}
J1155+5739	-154 ⁺¹⁴ ₋₁₄	161 ⁺¹⁸ ₋₁₈	0.7 ^{+0.2} _{-0.2}	-144 ⁺⁵ ₋₅	73 ^{+0.1} _{-0.1}	2.2 ^{+0.02} _{-0.02}
J1200+2719	-318 ⁺³⁵ ₋₃₅	315 ⁺³⁵ ₋₃₅	0.9 ^{+0.3} _{-0.3}	-143 ⁺⁵ ₋₅	82 ^{+0.1} _{-0.1}	...
J1215+2038	No Outflow	No Outflow
J1219+1526	-447 ⁺³¹ ₋₃₁	584 ⁺¹⁵¹ ₋₁₅₁	1.8 ^{+0.3} _{-0.3}	-310 ⁺⁷ ₋₇	182 ⁺² ₋₂	2.7 ^{+0.04} _{-0.04}
J1222+0434	No Outflow	No Outflow
J1226+0415	-269 ⁺¹⁸ ₋₁₈	310 ⁺¹⁰⁷ ₋₁₀₇	0.5 ^{+0.3} _{-0.3}	-125 ⁺⁵ ₋₅	64 ^{+0.1} _{-0.1}	1.8 ^{+0.05} _{-0.05}
J1230+1202	No Outflow	No Outflow
J1244+0215	-306 ⁺⁶⁵ ₋₆₅	357 ⁺¹⁴⁰ ₋₁₄₀	1.1 ^{+0.5} _{-0.5}	-224 ⁺⁵ ₋₅	140 ⁺¹ ₋₁	2.2 ^{+0.05} _{-0.05}
J1248+1234	-408 ⁺⁶² ₋₆₂	386 ⁺¹¹³ ₋₁₁₃	1.2 ^{+0.4} _{-0.4}	-202 ⁺⁷ ₋₇	110 ⁺² ₋₂	1.7 ^{+0.05} _{-0.05}
J1311-0038	-185 ⁺⁵⁵ ₋₅₅	147 ⁺⁶² ₋₆₂	1.3 ^{+0.2} _{-0.2}	-148 ⁺⁵ ₋₅	86 ⁺² ₋₂	...
J1416+1223	-441 ⁺¹¹ ₋₁₁	649 ⁺²¹⁶ ₋₂₁₆	1.5 ^{+0.2} _{-0.2}	-367 ⁺¹² ₋₁₂	212 ⁺¹ ₋₁	2.8 ^{+0.01} _{-0.01}
J1424+4216	-431 ⁺²² ₋₂₂	522 ⁺¹⁰⁴ ₋₁₀₄	1.6 ^{+0.3} _{-0.3}	-340 ⁺⁷ ₋₇	221 ⁺⁴ ₋₄	...
J1448-0110	No Outflow	-233 ⁺⁵ ₋₅	134 ⁺³ ₋₃	...
J1457+2232	-160 ⁺¹⁴⁰ ₋₁₄₀	249 ⁺¹¹⁶ ₋₁₁₆	1.2 ^{+0.3} _{-0.3}	-200 ⁺⁵ ₋₅	114 ⁺² ₋₂	2.2 ^{+0.06} _{-0.07}
J1509+3731	-134 ⁺⁴¹ ₋₄₁	126 ⁺⁵⁵ ₋₅₅	0.7 ^{+0.2} _{-0.2}	-112 ⁺⁵ ₋₅	55 ^{+0.1} _{-0.1}	...
J1735+5703	-244 ⁺⁶⁸ ₋₆₈	260 ⁺⁷² ₋₇₂	0.3 ^{+0.3} _{-0.3}	-238 ⁺⁸⁽²⁾ ₋₈	140 ⁺⁴ ₋₄	...

Note. –

(1) For UV absorption lines, we show the maximum outflow velocity (v_{95}^{out}), velocity widths (FWHM^{out}), and electron number density (n_e) by considering the median of all available UV lines that passed the F-test. For emission lines, we show similar properties, measured from H α (for v_{95}^{out} and FWHM^{out}) and [S II] $\lambda\lambda 6717, 6732$ doublet (for n_e) when available. Galaxies with no detections of outflows are labelled as ‘No Outflow’. See details of the measurements in Sections 3.3 and 4.4.

(2) This galaxy’s H α emission line is in a detector gap, so we report the values from H β .

natures are consistently detected using both diagnostics, i.e., whenever an outflow component is required for the absorption line, the galaxy also needs the broad component to fit its emission line. This happens for 27 out of 33 galaxies. For a few cases when no clear outflow features are seen in the absorption, the optical lines are indeed narrower and show no broad wings (J1129+2034, J1215+2038, J1222+0434, J1230+1202). Two other exceptions are J0808+1728 and J1448-0110, whose Si II and C II absorption lines show no outflow signatures but whose H α emission lines still require the broad component. For J1448-0110, however, we do detect blue-shifted absorption in its Si IV doublet lines. Thus, it is likely that galactic outflows in this galaxy are highly ionized, and undetectable in low-ionization lines (see a few similar cases in Grimes et al. 2009; Martin et al. 2015). Unfortunately, no data exist for J0808+1728’s Si IV region. Future larger samples with similar objects will provide more information.

Overall, there is clear evidence that the existence of broad components seen in emission and absorption lines are linked in the majority of our galaxies (> 94%) and they represent galactic outflows. We will discuss their correlations more quantitatively in Section 4.

3.3. Line Measurements

After extracting the broad components from the absorption and emission lines, we conduct various measurements of the line properties. To make a fair comparison for outflows, we focus on the blue-shifted, broad component ($v < 0$ km s $^{-1}$) of the emission lines. This is because the absorption lines can only trace the gas along the line-of-sight (LOS), so we normally cannot detect the gas that is moving away from us (i.e., the redshifted side of the outflows). Thus, it is preferable to separate them when comparing with the blue-shifted, broad component in absorption lines.

For each emission line, we first measure its best-fitted broad component flux and line width for the blue-shifted half. For the latter, we call it “half-width-half-maximum (HWHM)” of the broad component. Then we measure the cumulative flux of this blue-shifted half as (e.g., Whittle 1985):

$$\Phi(v) = \int_v^0 F(v') dv'; \quad (v < 0) \quad (1)$$

where $F(v')$ is the line normalized flux at a velocity, and the integration is over blue-shifted velocities. After that, we can define v_a^{out} representing the outflow velocity when $\Phi(v) = \frac{a}{100} \times \Phi(-\infty)$ (Liu et al. 2013), i.e., the velocity at which the cumulative flux in the broad component reaches a certain percentage of the blue-shifted,

broad component flux. Specifically, we calculate v_a^{out} for $a = 95, 90, 50, 10,$ and 05 . We adopt v_{95}^{out} to represent the maximum outflow velocity of the line.

Additionally, we quantify the asymmetry of the broad component of emission lines with respect to $v = 0$. We first calculate another set of v_a values as follows. For the best-fit full, broad component of each emission line, we integrate Equation (1) again with the upper integration range to be $+\infty$. Then we calculate the A_{90} parameter (Liu et al. 2013; Martin et al. 2015):

$$A_{90} = \frac{(v_{90}^{f,b} - v_{50}^{f,b}) - (v_{50}^{f,b} - v_{10}^{f,b})}{v_{90}^{f,b} - v_{10}^{f,b}} \quad (2)$$

where a positive (negative) value of A_{90} means the line contains more flux on the blue-shifted (red-shifted) side. The notation ‘f,b’ means that we adopt the full, broad component of the emission line. We find all of our galaxies have quite small A_{90} values ($\lesssim 0.01$)⁴, which suggests the broad component of emission lines representing the outflows are close to symmetric around $v = 0$.

For the above parameters, we estimate the corresponding errors through a Monte Carlo (MC) simulation where we perturb the spectrum 10^3 times according to the observed 1σ uncertainties. The detection rates of broader but weaker outflow components in emission lines have been found to be dependent on SNR (see discussion in Section 5.3). Thus, in Table 2, we report the measurements from our strongest line, i.e., H α . When H α is contaminated by telluric features, we report measurements of H β instead. We will adopt these measurements of H α in the rest of the paper when compared with the ones from UV absorption lines.

Similarly, for each diagnostic absorption line in the UV, we measure the FWHM $^{\text{out}}$ and v_a^{out} values from the fitted broad component (Section 3.2.1). For the latter, we integrate the optical depth instead of flux in Equation (1) (Xu et al. 2020). For each galaxy, we calculate their median FWHM $^{\text{out}}$ and v_a^{out} accounting for all absorption lines that passed the F-test. Unlike emission lines, since all absorption lines for a certain galaxy have similar SNRs, the median values are more representative of all absorption features (Xu et al. 2022a). We report these measurements in the 2nd and 3rd columns in Table 2. We have already corrected the listed FWHM and HWHM values by subtracting the instrumental resolution in quadrature.

3.4. Ancillary Measurements

⁴ For a reference, for AGN outflows, where strong blue-shifted emission lines are commonly seen. Their broad components were found to have $A_{90} = 0.1$ to 0.4 in our definition (Liu et al. 2013).

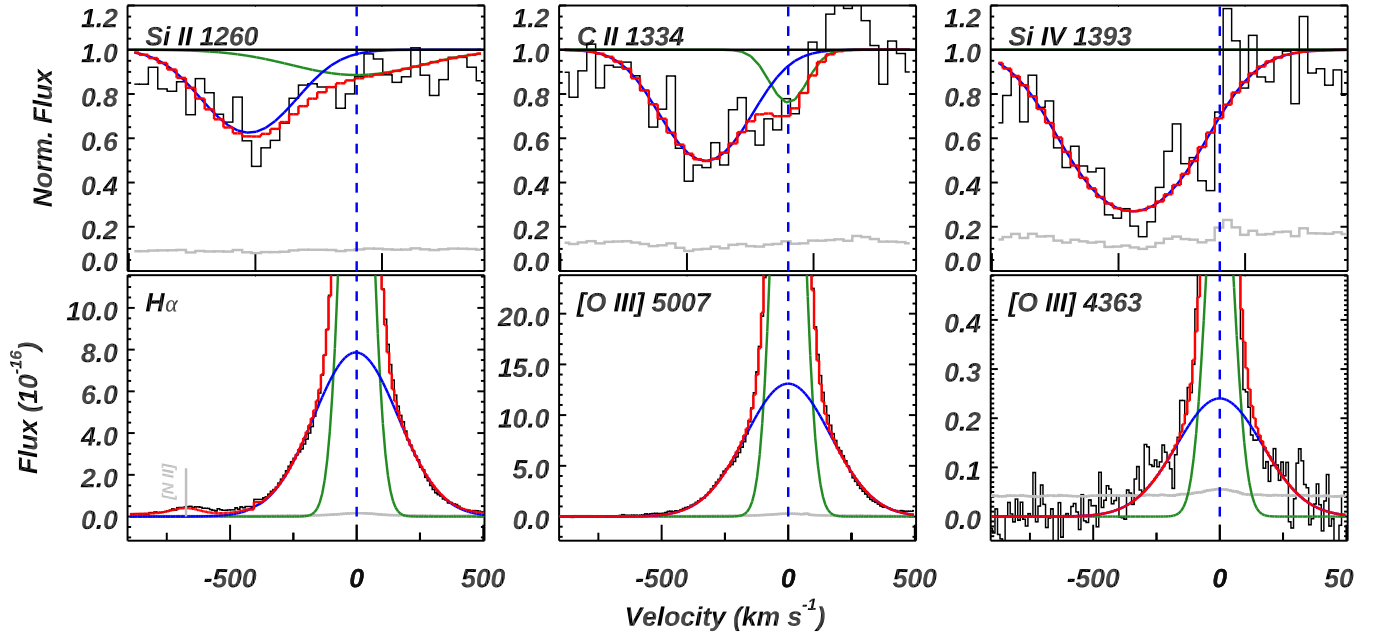


Figure 2. Spectral line fitting for one galaxy (J0926+4427) in our sample. Other galaxies are shown in Appendix A. The flux and uncertainties are shown in black and gray histograms, respectively. The flux unit for emission lines is $\text{ergs s}^{-1} \text{cm}^{-2} \text{\AA}^{-1}$, while absorption lines are shown in normalized flux. For each line, the best-fit narrow and broad components are shown in green and blue, respectively. The red line is the summation of all models. Line fitting details are discussed in Section 3.2.

To quantify the spatial extent of starburst regions, we measure galaxy starburst sizes (r_*) from HST/COS data. We first calculate the UV half-light radius of each galaxy from its COS NUV acquisition images following Xu et al. (2022b). In short, we accumulate the net photon counts within a certain radius from the center of a galaxy until it reaches half of the total source counts. For galaxies that are more spatially extended than the unvignetted size of the COS aperture ($r \sim 0.4''$), we treat their measured r_{50} as lower limits. We adopt these measured r_* to derive UV outflow spatial extension in Section 4.3.

For each galaxy, we find their Milky Way dust extinction using the Galactic Dust Reddening and Extinction Map (Schlafly & Finkbeiner 2011) from the NASA/IPAC Infrared Science Archive. We then calculate the internal dust extinction ($E(B - V)_{\text{int.}}$) for each galaxy from a set of Balmer lines (i.e., $H\alpha + H\beta + H\gamma$) following the methods in Xu et al. (2022a).

Since SFR estimates from SED fitting covary with other fit parameters such as metallicity, dust, and age, we instead derive SFR based on the full $H\alpha$ emission line, which stands for SFR within the slit. After correcting for Balmer absorption using the SED fitting results and the dust extinction, we adopt a metallicity-dependent calibration for inferring SFR from $H\alpha$ luminosity (Strom et al. 2017, and Korhonen Cuestas et al. in prep.). When $H\alpha$ is not available, we adopt the dust-

corrected $H\beta$ luminosity $\times 2.86$ into the calculations. All ancillary parameters are reported in the table of Appendix C.

4. CONNECTING OUTFLOW PROPERTIES FROM UV AND OPTICAL DIAGNOSTICS

4.1. General Justification

Absorption and emission lines provide us with distinct approaches to investigate the outflowing gas. From the last two decades, well-established methods have been developed to measure galactic outflow properties from absorption (e.g., Rupke et al. 2002; Martin 2005; Steidel et al. 2010; Heckman et al. 2015; Chisholm et al. 2018; Prusinski et al. 2021; Xu et al. 2022b) and emission lines (e.g., Genzel et al. 2011; Newman et al. 2012b; Soto & Martin 2012; Freeman et al. 2019; Swinbank et al. 2019; Perna et al. 2020; Perrotta et al. 2021; Amorín et al. 2024; Carniani et al. 2024; Weldon et al. 2024). However, it is surprising that we are still unclear if and how the outflow properties derived from the two diagnostics are connected.

Theoretically, the ions studied here using absorption and emission lines (Section 3) probe similar temperatures of warm-ionized gas ($T \sim 10^4$ K). Since the absorption line's column density scales with gas density ($\propto n$) and the emission line's luminosity scales with density squared ($\propto n^2$), these two types of outflow measurements are thought to be weighted towards different re-

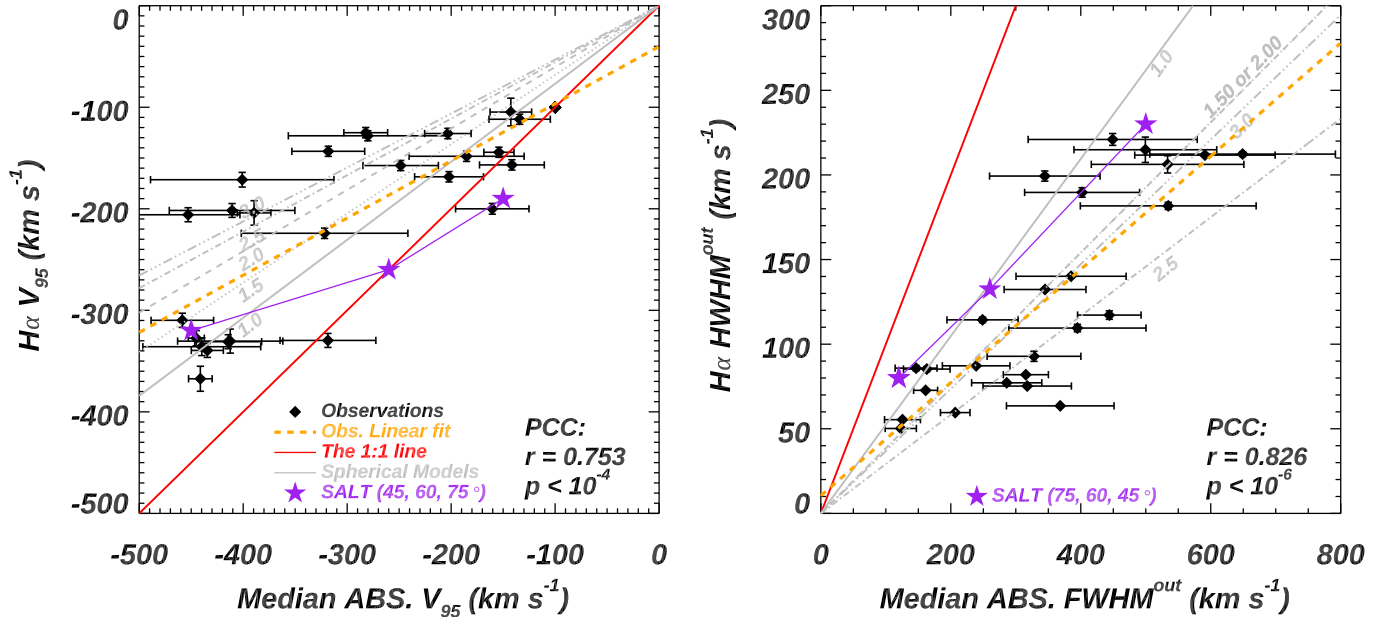


Figure 3. Correlations of the outflow kinematics derived from absorption and emission lines for the same galaxy. **Left:** For emission lines, we report v_{95}^{out} from the highest SNR line, i.e., H α . For absorption lines, we report the median v_{95}^{out} measured from all absorption lines that contain outflowing features. Each symbol corresponds to one galaxy, and the bars indicate the error sizes. The red line denotes the 1:1 relationship. **Right:** Similarly as the left but for outflow velocity widths. For emission lines, we only measure the width of the blue-shifted portion of emission lines (i.e., HWHM^{out}) to make a fair comparison with that of blue-shifted absorption lines. In both panels, we show the best linear fit as the orange dashed lines. We overlap spherical outflow models with different outflow density distributions $n(r) \propto r^{-\gamma}$ in gray lines, where the line styles and the labelled γ values are the same as the ones in Figures 5 and 6. We also overlay bi-conical outflow models from SALT (Carr et al. 2023) in purple stars given M 82 galactic outflow parameters, where the three stars represent different orientation angles listed in the parentheses from the left to right. We discuss the model details in Section 5.1.

gions of the outflow. If both outflows are dominated by similar driving mechanisms (in our case, by the energy and momentum from SF regions), we would hypothesize that the outflow properties from the two diagnostics should be connected.

Given the high-quality UV + optical data for the galaxies in our sample, we next investigate this hypothesis and the possible connections between outflow properties measured from the two different diagnostics. We start by comparing the outflow kinematics in Section 4.2. Then we present the links between outflow sizes in Section 4.3 and outflow densities in Section 4.4.

4.2. Outflow Kinematics

For galaxies with detected outflows in both emission and absorption lines, we start by comparing the maximum outflow velocity (v_{95}^{out}) derived from the two diagnostics. We choose to use v_{95}^{out} instead of the central velocity (v_c) of a line. This is because v_c is normally quite close to zero for emission lines, given the fact that we can detect emission from both blue- and red-shifted sides of the outflows. On the contrary, $v_c \ll 0$ for all absorption lines since we can only detect them in the foreground of the galaxies.

The comparison of v_{95}^{out} is shown in the left panel of Figure 3. It is clear that there is a significant correlation; the Pearson correlation coefficient (PCC) p-value is $< 10^{-4}$. The v_{95}^{out} values measured from emission lines are similar to the ones measured from absorption lines for weak outflows ($100 < v_{95}^{\text{out}} < 200 \text{ km s}^{-1}$), but are smaller for stronger outflows. We show the best linear fit in the orange dashed line as:

$$v_{95}^{\text{out}}(\text{H}\alpha) = (0.56 \pm 0.1) \times v_{95}^{\text{out}}(\text{ABS.}) - (40 \pm 30) \text{ km s}^{-1} \quad (3)$$

which yields a shallower slope compared to the 1:1 correlation in the red solid line.

In the right panel of Figure 3, we show the line widths measured from outflow emission and absorption lines in the same manner. As illustrated in Section 3.3, we adopt the HWHM^{out} of emission lines in the comparison since this represents the blue-shifted portion of the emission that coincides with the blue-shifted absorption lines. In this case, we also find a tighter correlation with a p-value $< 10^{-6}$. HWHM^{out} from emission lines are typically smaller than the FWHM^{out} measured from absorption lines, where the best linear fit yields:

$$\begin{aligned} \text{WHM}_{95}^{\text{out}}(\text{H}\alpha) &= (0.33 \pm 0.04) \times \text{FWHM}_{95}^{\text{out}}(\text{ABS.}) \\ &+ (10 \pm 18) \text{ km s}^{-1} \end{aligned} \quad (4)$$

In Figure 3, we also overlay two different sets of model predictions. This includes the spherical models with different outflow density distributions (see Equations 9) in gray lines and bi-conical outflow models given M 82 parameters in purple stars. We discuss these models in details in Section 5.1. In short, we find our models can well explain the observed correlations.

4.3. Outflow Spatial Extensions

It is critical to understand whether outflows seen in absorption or emission lines originate from similar spatial scales. Thus, we estimate the outflow sizes (R^{out}) from UV and optical spectra separately. For UV absorption lines, given the measured starburst size (r_*) from the COS NUV acquisition image (Section 3.4) for each galaxy, we calculate $R_{\text{UV}}^{\text{out}}$ based on the correlation given by Xu et al. (2023b):

$$\log(R^{\text{out}}) = 0.822 \times \log(r_*) + 0.583 \quad (5)$$

where R^{out} and r_* are in units of kpc. This is based on the assumption that the observed outflows are in pressure equilibrium with the hot wind fluid.

For galaxies with Keck/ESI long-slit spectra, we measure outflow sizes from the broad H α emission lines as follows. We first extract the spectra in thin boxes at different locations along the cross-dispersion direction, starting from the center of the trace. Each thin box is chosen to cover the H α + [N II] wavelength regions with a width of 2 pixels in the cross-dispersion direction. Then we conduct the Gaussian spectral line fitting to the spectra from each box, adopting the same methodology in Section 3.2.2. This allows us to calculate the relative strengths of the broad and narrow components at different spatial locations in the cross-dispersion direction. In turn, we can construct the 2D modeled spectra of the broad and narrow components separately. After that, we convert the measured H α flux in the broad component to surface brightness (SB) and calculate the radius enclosing half of the total integrated SB (i.e., $\int SB(r) \times 2\pi r dr$). This assumes the outflow SB(r) measured from the broad components are spherically symmetric. Finally, we subtract half of the average seeing ($0''7/2 = 0''35$) in quadrature from the resulting radius. In cases where we find radius is less than $0''35$, we consider the outflows unresolved and report the measured outflow radius (R^{out}) as an upper limit.

In Figure 4, we compare the two sets of R^{out} derived above, where we find a strong positive correlation with a p-value $\sim 6 \times 10^{-3}$. The lower and upper limits are shown as arrows, while the 1:1 relationship is in red to guide the eyes. The best linear fit is shown as the orange dashed line, which has the form as:

$$\begin{aligned} \log[R_{\text{OPT}}^{\text{out}}] &= (0.63 \pm 0.2) \times \log[R_{\text{UV}}^{\text{out}}] \\ &- (0.43 \pm 0.10) \text{ kpc} \end{aligned} \quad (6)$$

On average, we find $R_{\text{OPT}}^{\text{out}}$ is $\sim 2 - 5$ times smaller than $R_{\text{UV}}^{\text{out}}$. This is consistent with the fact that emission line strengths are weighted towards higher density regions, i.e., $\propto n^2$ versus $\propto n$ for absorption lines. Thus, the observed emission line fluxes should be dominated by gas that is closer to the centers of the galaxies. We also find this matches our model predictions described in Section 5.1.

4.4. Outflow Density

Outflow electron number density (n_e) is another critical parameter that determines the observed line profiles of the outflowing gas. For emission lines, we follow the commonly adopted method to constrain n_e of the low-ionization zone (Mingozzi et al. 2022), based on the density-sensitive lines of [S II] $\lambda\lambda 6717, 6731$. Here, we are able to isolate the outflow n_e by measuring only the blueshifted, broad component of emission lines. We adopt *PyNeb* and calculate electron temperature (T_e) from [O III] 4363/([O III] 4959 + 5007) simultaneously (e.g., Berg et al. 2022). The errors are calculated using MC simulations by perturbing the input line flux 10^3 times according to the observed 1σ uncertainties. In total, we have 15 galaxies that have a clean, measurable [S II] doublets.

For outflows detected in absorption lines, Xu et al. (2023b) have shown that R^{out} and n_e are correlated in local SF galaxies. Given earlier assumption that we take in Section 4.3, i.e., detected outflows in UV are in pressure equilibrium with the hot wind fluid, we have:

$$n_{e, \text{UV}} = \frac{\dot{p}_{\text{SFR}}}{8\pi(R_{\text{UV}}^{\text{out}})^2 kT} \quad (7)$$

where \dot{p}_{SFR} is the total momentum flux of the hot wind that can be estimated given SFR (Heckman et al. 2015), k is the Boltzmann constant, and $T = 10^4$ K is the assumed temperature. The measured n_e values are listed in Table 2.

In the right panel of Figure 4, we compare the two sets of outflow densities derived from absorption and emission lines. It is evident that n_e from the [S II] emission lines is consistent with being larger than n_e from

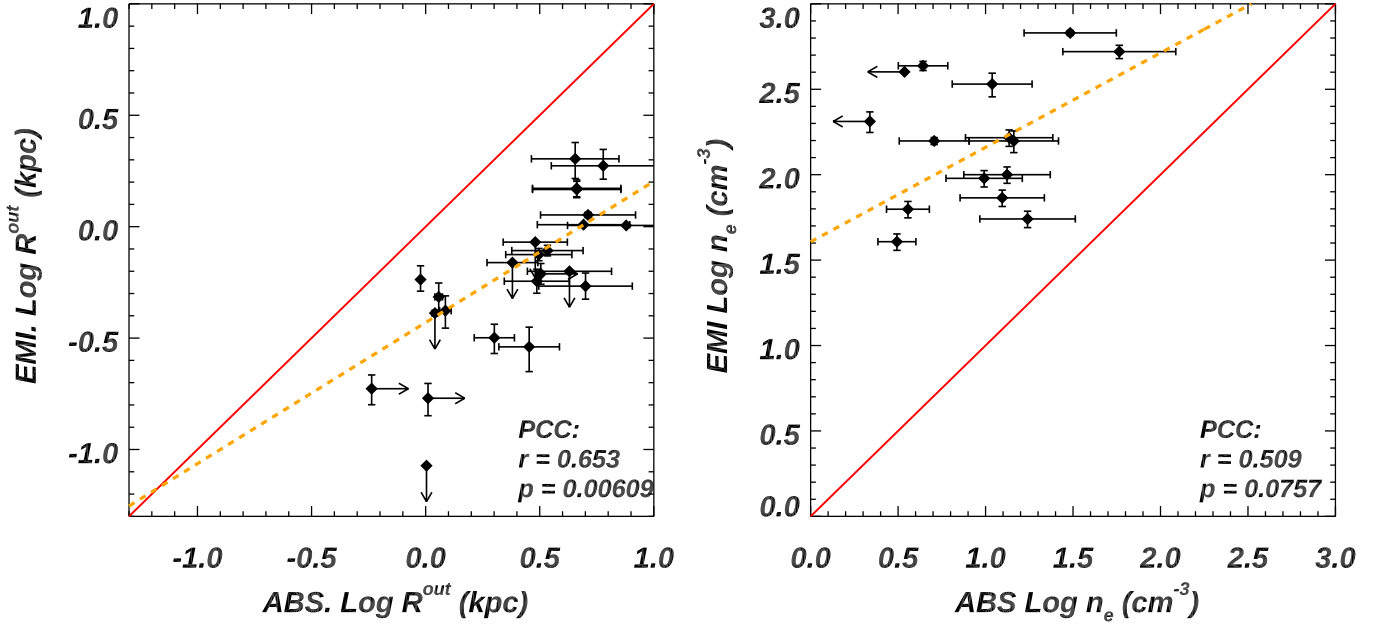


Figure 4. Same as Figure 3 but for comparing the outflow spatial extensions (**Left**) and outflow density (**Right**). Values in both axes are in logarithm scales. The red line is the 1:1 relationship to guide the eyes. It is evident that the outflow components in emission lines are weighted towards smaller R^{out} regions and higher n_e than that of absorption lines in the same galaxy.

absorption lines in all cases. This is again a direct expectation from the $\propto n^2$ scaling for emission lines versus $\propto n$ scaling for absorption lines. However, we don't find a strong linear correlation between the two sets of n_e . This is likely because n_e is spatially dependent and the measured densities from unresolved spectra have more uncertainties due to, e.g., orientation of the outflows to the LOS and the slope of $n(r)$ distribution. Future spatially resolved observations and simulations of galactic outflows will provide more insights on this problem.

5. DISCUSSION

5.1. Outflows in Emission and Absorption Lines from Analytical Models

5.1.1. Simple Analytical Models of an M82-like Galactic Wind

Given the empirical correlations presented in Section 4, it is important to check if they are consistent with the predictions from models of galactic outflows. In an idealized case, we assume the outflows consist of spherically expanding thin shells with certain velocity and density fields, i.e., $v(r)$ and $n(r)$, for which we adopt (e.g., Chisholm et al. 2017):

$$v(r) = v_\infty (1 - R_{\text{SF}}/r)^\beta \quad (8)$$

where v_∞ is the terminal velocity of outflows, β is the power index, and R_{SF} is the launch radius of the outflow, which we assume it equals the size of the star-forming region. We start with $v_\infty = 800 \text{ km s}^{-1}$, $R_{\text{SF}} = 300 \text{ pc}$,

and $\beta = 1$ to approximate the observed galactic outflow velocity distribution seen in M 82 (Xu et al. 2023a).

Similarly for $n(r)$, we take values that match the observations of M 82 as:

$$\begin{aligned} n(r) &= n_0 (R_{\text{SF}}/r)^\gamma \\ ff(r) &= ff_0 (R_{\text{SF}}/r)^\delta \end{aligned} \quad (9)$$

where $n_0 = 372 \text{ cm}^{-3}$ is the observed outflow density at R_{SF} and $ff(r)$ is the volume-filling factor, which represents how much volume filled by the $\text{H}\alpha$ emitting gas. Spatially resolved studies of galactic outflows in M 82 yield $\gamma = 1.17$, $ff_0 = 0.378\%$ and $\delta = 1.8$ (Xu et al. 2023a). Then the predicted flux of $\text{H}\alpha$ from each shell is:

$$\begin{aligned} dF_{\text{H}\alpha}(r) &\propto n(r)^2 ff(r) \times d\text{Vol}(r) \\ &= n(r)^2 ff(r) \times 4\pi r^2 dr \end{aligned} \quad (10)$$

where $\text{Vol}(r)$ is the volume of a shell at r . It can also be shown that, for a spherically symmetric outflow, this flux is evenly distributed between $[-v(r), +v(r)]$ (e.g., Peng et al. submitted). Thus, we get:

$$\frac{dF_{\text{H}\alpha}(r)}{dv} = \frac{n(r)^2 ff(r) \times 4\pi r^2 dr}{2v(r)} \quad (11)$$

The dF/dv values for each shell are shown as the colored lines in the left panel of Figure 5 for M 82 outflows. The sum of the emission from all shells is shown in the

thick black line. The summation goes from $r = 0.3 - 2.2$ kpc to match the range adopted in Xu et al. (2023a) for M 82. We present the measured HWHM^{out} and v_{95} in the top-right corner. It can be seen that the $\text{H}\alpha$ emission line flux is clearly dominated by the shells at small radius (i.e., in purple colors). This is as expected since these shells have the highest density and the $\text{H}\alpha$ flux is proportional to n^2 .

In the right panel, we further compare models with different choices of γ from 1.0 to 3.0, standing for $n(r) \propto r^{-1}$ to r^{-3} . It is apparent that the modeled line profiles become more concentrated towards the lower velocities given higher γ values. The measured HWHM^{out} also decreases from 180 km s^{-1} to 100 km s^{-1} and v_{95} drops from -520 km s^{-1} to -310 km s^{-1} given the increasing γ values. Note that in all cases, we do not include the static ISM components, which can be comparable to, or stronger than, the outflow components.

Under the same assumptions, we can also estimate the outflow absorption lines profiles. In this sample model, we only consider the absorption but not the scattering. Then we can write down the cross section of an absorption line as:

$$\sigma(\nu, r) = \sigma_0 \phi(\nu, r) = \frac{\pi e^2}{m_e c^2} f \phi(\nu, r) \quad (12)$$

where e is the electron charge, m_e is the electron mass, c is the speed of light, f is the oscillator strength of the transition (which we assume Si II $\lambda 1260$ hereafter), and $\phi(\nu, r)$ is the line profile function, which is dependent on both the frequency ν and shell radius r . Then we take the Doppler broadening in a Gaussian profile as:

$$\phi(\nu, r) = \frac{1}{\sqrt{\pi} \Delta \nu_D} \exp\left(-\frac{(\nu - \nu_0)^2}{(\Delta \nu_D)^2}\right) \quad (13)$$

where ν_0 is the central frequency of the line⁵, and $\Delta \nu_D$ is the Doppler width. Then we can get the optical depth velocity distribution as:

$$\tau(v) = \int n_{\text{ion}}(r) \sigma(v, r) dr \quad (14)$$

where we adopt the same integration range ($r = 0.3 - 2.2$ kpc) as we used for calculating the emission lines profiles, and $n_{\text{ion}}(r)$ is the ion number density. For Si II, we adopt $n_{\text{Si II}}/n_{\text{H}} \sim 10^{-6.5}$ in local SF galaxy outflows (Xu et al. 2022b). Finally, we can calculate the normalized flux for absorption lines assuming a full coverage model:

⁵ The frequency ν is mapped to the wavelength given $\lambda = c/\nu$. For a certain line, λ is then mapped to the velocity (v) according to the relativistic Doppler effect.

$$I/I_0 = e^{-\tau(v)} \quad (15)$$

The resulting optical depth and absorption line profiles are shown in Figure 6. For $\tau(v)$, we also draw the contributions from each shell in the same color schemes as emission lines in the left panel of Figure 5. We find that the absorption lines are clearly broader and reach higher velocities than the emission lines. This is because we can still detect significant absorption at higher velocities that are dominated by outer shells. On the contrary, the emission from these outer shells are negligible as seen in Figure 5. This difference is mainly because emission lines are naturally dominated by the higher density regions than absorption lines.

Additionally, we compare modeled outflow absorption lines profiles with different γ values in Figure 7. The model with a larger γ results in more column densities at lower velocities. We notice the models with $\gamma \sim 2$ match better with the observed UV absorption troughs (see Figure 12), since we do not detect excessive outflow absorption in either the lowest or highest velocities in any of our galaxies.

To further quantify the similarities between observations (Section 4) and models of outflow absorption and emission lines, we overlay the modeled results into Figures 3 and 9 as the gray lines. Each line represents a set of models with the same γ but different v_∞ values. We find the model with $\gamma \sim 2.0$ is on-average the best match to both the overall correlations in maximum outflow velocity and line widths. But there are also galaxies consistent with significantly smaller (~ 1) or larger (~ 3) γ values. This is likely because the simplicity of our models here, which have ignored several factors, e.g., outflow opening angle and orientation. We consider them in a more sophisticated model in Section 5.1.2.

Overall, we conclude that our simple spherical shell models can qualitatively reproduce the observed kinematic correlations between outflows seen in emission and absorption lines, i.e., we expect that the same outflow radial and density distributions produce emission lines with narrower line widths and lower maximum velocities compared with the absorption lines. In addition, the relative strengths from different shells (colored lines in Figures 5 and 6) also suggest that emission lines are more dominated by shells at smaller radii and have higher densities than those of the absorption lines. These match what we observe in Figure 4. We also highlight the fact that one can use the correlations (e.g., Equations 3, 4, 6, and 16) to estimate the properties of the outflow absorption lines from the emission lines and vice versa.

5.1.2. SALT Models of Galactic Outflows

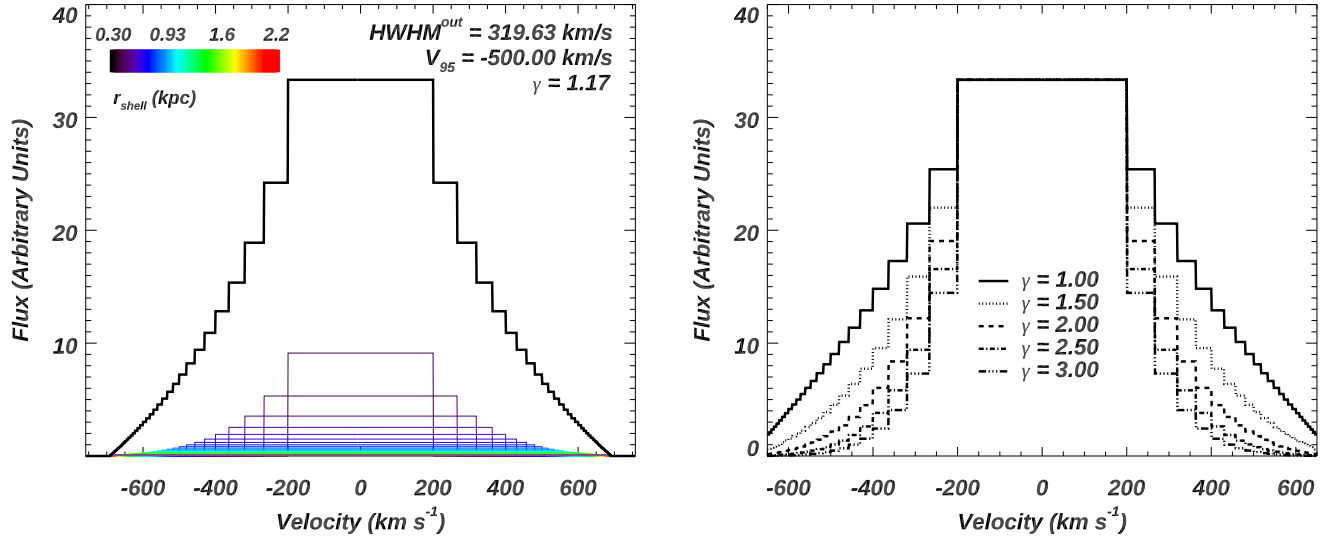


Figure 5. Modelled $\text{H}\alpha$ outflow emission line profiles assuming spherical expanding shells for galactic outflows. **Left:** We adopt the observed radial distributions of velocity, density, and volume filling factor that are measured from M 82 galactic outflows (Xu et al. 2023a). The $\text{H}\alpha$ emission from each shell at a certain radius is shown as a rectangle with different colors, while the sum of emission from all shells is shown in a thick black line. The measured half-width-half-maximum (HWHM^{out} , see Section 4.2) of the line and V_{95} of the blue-shifted emission are listed at the top-right corner. We do not include the static ISM component in these models. **Right:** Same as the left panel but we compare the results given different outflow density profiles $n(r) \propto r^{-\gamma}$. A steeper $n(r)$ distributions yield narrower emission line profiles. See more discussions in Section 5.1.1.

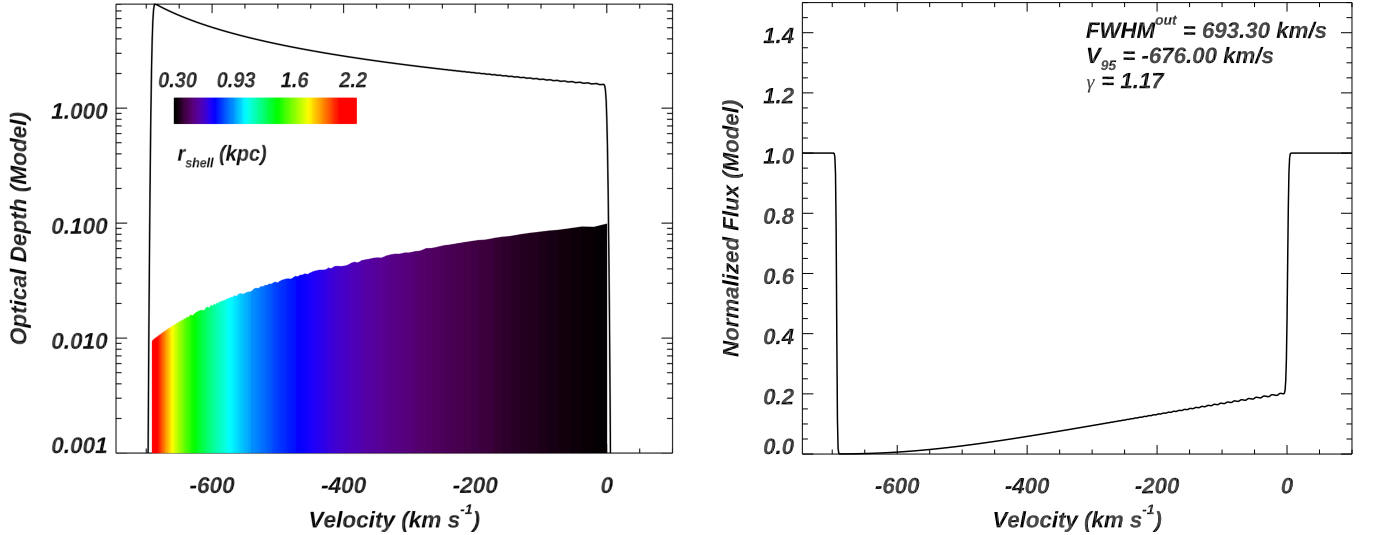


Figure 6. Absorption line profiles assuming the same spherical outflow settings as the left panel of Figure 5. **Left:** Absorption line optical depths from each shell are shown in different colors. The black line is the summed optical depth. **Right:** Normalized flux calculated given the optical depth in the left panel. It is clear that the gas produce outflow absorption lines with broader line width and larger maximum velocity than those in emission lines. These trends are consistent with our observed correlations in Section 4. See discussion in Section 5.1.1.

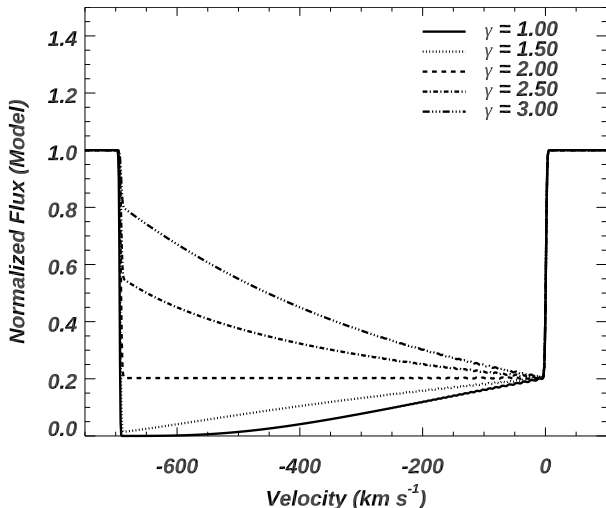


Figure 7. Same as Figure 6 but we compare the outflow absorption line profiles given different outflow density profiles $n(r) \propto r^{-\gamma}$. A steeper $n(r)$ distributions yield more column densities piled up at lower velocity. See discussion in Section 5.1.1.

In reality, we know the hot galactic wind and warm outflows in M 82 are not totally spherical symmetric but more close to bi-cones (e.g., Shoppell & Bland-Hawthorn 1998; Xu et al. 2023a). This is not uncommon among SF galaxies (Burchett et al. 2021; Carr et al. 2021). Furthermore, Xu et al. (2022b) found the high detection rates of outflows in local SF galaxies suggest they cover large fractions ($\sim 90\%$) of the galaxy’s solid angle. These do not conflict with the bi-cone geometry, but instead suggest the opening angle of the cone should be large for local SF galaxies.

As such, wind geometry can also affect the appearance of the emission and absorption line components. For instance, a bi-cone oriented perpendicular or parallel to the line of sight can result in an emission or an absorption profile, respectively, and the observed velocities are projected (Carr et al. 2018). Here we explore the implications of the bi-conical wind geometry observed in M 82 on the resulting line profiles using an adaptation of the Semi-analytical Line Transfer (SALT) model presented in Carr et al. (2023). In particular, we adapt SALT to allow for the velocity field described in Equation 8 and develop a new feature in SALT to account for *in situ* H α emission emanating from the bi-cone. In all calculations, we also adopt the same density profile and initial parameters (e.g., v_∞ , R_{SF} , and n_0) as the model described in Section 5.1.1. The detailed models are illustrated in Appendix B.

We show the resulting absorption and emission line profiles in Figure 8, where we assume the outflow has a half-opening angle of 37° and the bi-cone is oriented

at 75° away from the line of sight as observed in M 82 (Shoppell & Bland-Hawthorn 1998; Xu et al. 2023a). This orientation results in a low covering fraction and shallow absorption trough. On the other hand, the orientation favors a prominent H α emission spike roughly centered on velocity = 0⁶. We then measure these line profiles using the same method in Section 3.3 and overlay the results as the purple stars in Figure 3. We similarly show results with two additional bi-cone orientations (60° and 45°) with other parameters the same as M 82. The order of them is listed in the parentheses.

We find SALT models show quite consistent results with our observed galaxies in the cases of 60° and 45° . When the bi-cone is oriented 75° away from the LOS (i.e., the true value for M 82), the modeled outflow velocity and widths are close to the margin of our observed galaxies. This is not surprising since none of our galaxies should have bi-cone outflow orientations close to that of M 82, which is too perpendicular to the LOS, so there is no background light to produce the absorption lines when observed from Earth.

This test provides an example where the outflow geometry can alter the observed outflow line profiles (especially absorption) for a specific galaxy, but measured outflow properties from emission and absorption lines are still in agreement with the empirical correlations found in Section 4. More robust fits of the models to each of our galaxies are beyond the scope of the paper, but we plan to investigate this topic further in a future publication.

5.2. Other Studies of Comparing Outflow Diagnostics

In Figure 9, we compare our results with previous studies of warm-ionized galactic outflows given both the optical emission and UV absorption line diagnostics. In this case, we show FWHM^{out} (instead of HWHM^{out} in Figure 3), which is to match the common line width measurements adopted in the literature. All symbols and lines are the same as Figure 3 except the blue and pink ones from the literature as follows.

We first show NGC 7552 reported in Wood et al. (2015) in blue symbol. It is a barred spiral galaxy with $\log M_\star = 10.52 M_\odot$ and $\text{SFR} = 13 - 47 M_\odot/\text{yr}$ (Sheth et al. 2010; Pan et al. 2013). Wood et al. (2015) find the broad components in H α (FWHM^{out} up to 380 km s^{-1}) is much smaller than that from UV absorption lines, such as Si II, Si III, and Si IV ($\sim 800 \pm 100 \text{ km s}^{-1}$). This yields a bit lower H α FWHM^{out} than our trend, which suggests that H α FWHM^{out} would be $\sim 500 \text{ km}$

⁶ Unlike the spherical model in Section 5.1.1, a bi-conical model can produce outflow emission at $v = 0$ under certain orientations.

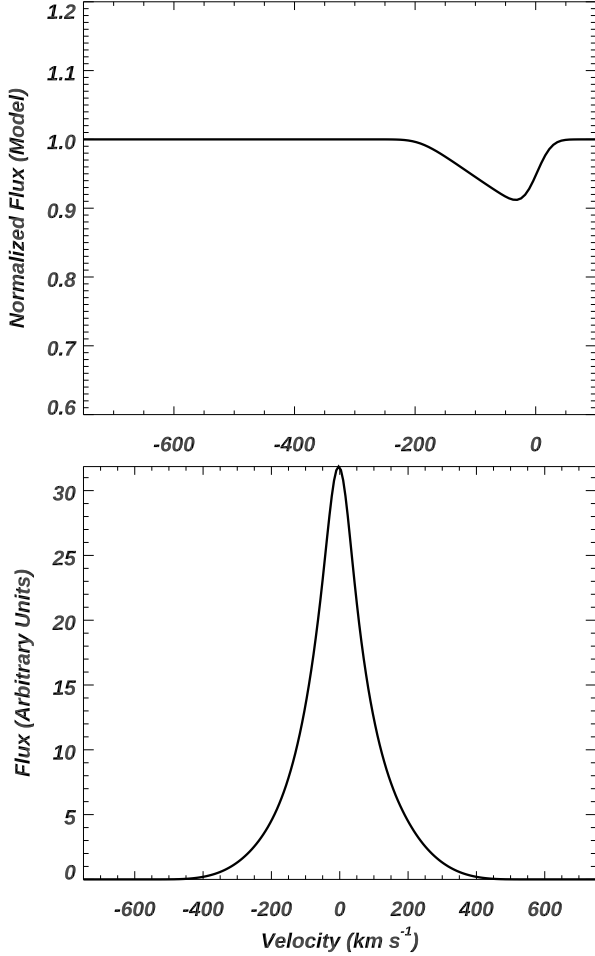


Figure 8. SALT model predictions of M 82-like galactic outflows. The top panel shows the absorption profile for Si II 1260Å line. Since M 82’s bi-conical outflow is oriented away from the line of sight by $\sim 75^\circ$ (Shopbell & Bland-Hawthorn 1998), the covering fraction is small resulting in a shallow absorption well. The bottom panel shows the H α line emanating from the outflow. Here, the orientation of the outflow results in a line profile with a single peak centered around zero velocity. See discussion in Section 5.1.2.

s^{-1} if UV $\text{FWHM}^{\text{out}} = 800 \text{ km s}^{-1}$. We also overlay several galaxies in Peng et al. submitted in pink colors. They are low-mass star-forming galaxies selected from the CLASSY sample with follow-up optical observations.

In general, we find galaxies from the literature exhibiting a consistent tight correlation with ours. Considering all galaxies shown in Figure 9, we have for warm-ionized outflows:

$$\begin{aligned} \text{FWHM}_{95}^{\text{out}}(\text{H}\alpha) &= (0.57 \pm 0.10) \times \text{FWHM}_{95}^{\text{out}}(\text{ABS.}) \\ &+ (60 \pm 30) \text{ km s}^{-1} \end{aligned} \quad (16)$$

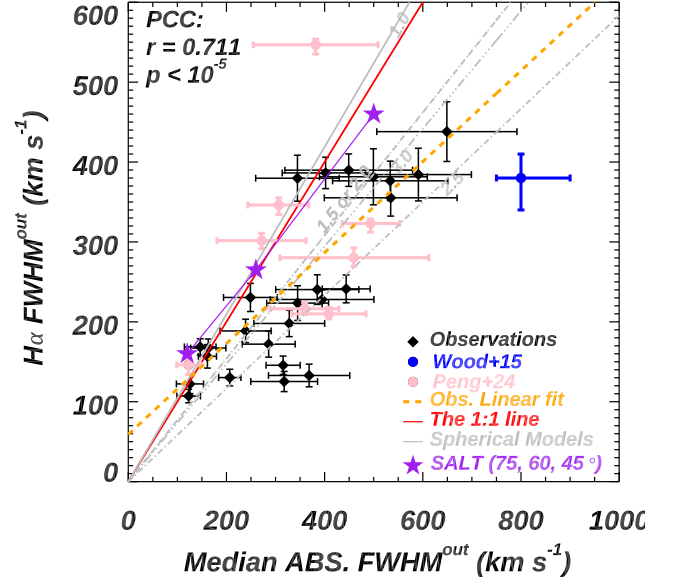


Figure 9. Same as the right panel of Figure 3 but the y-axis is FWHM^{out} instead of HWHM^{out} . We also overlay multi-diagnostic warm-ionized outflow detections from the literature in different colors. See discussion in Section 5.2.

Besides the warm-ionized outflows, there exist studies of less ionized and neutral outflowing gases. Soto & Martin (2012) studied a sample of 39 ultraluminous infrared galaxies (ULIRGs) at $z = 0.043 - 0.163$ using Keck ESI observations. They find that broad optical emission lines tracing galactic outflows span a velocity range quite similar to that of the blueshifted Na I absorption troughs seen in the same galaxies (Martin 2005, 2006). Unlike the ionized outflows studied in our work, Na I traces the neutral, dustier gas. Thus, their work suggests that the neutral outflowing gas detected from absorption lines may correlate with ionized gas seen in emission lines.

Perrotta et al. (2021) also briefly compared galactic outflows detected from emission and absorption lines in a sample of 14 massive ($M_\star \sim 10^{10} M_\odot$), compact starburst galaxies ($\Sigma_{\text{SFR}} = 5 - 1750 M_\odot/\text{yr}/\text{kpc}^2$) at $z = 0.4 - 0.7$. They find the maximum outflow velocity (in the form of V_{98}) measured from the [O II] emission line is always less than or equal to the ones measured from Mg II absorption lines in the same galaxy. This again is consistent with what we find in Figure 4.2. They do not provide further discussions.

Overall, we find that although connections between outflow signatures seen in optical emission and UV metal absorption lines have been noticed previously, no systematic studies were made until our current study. Our observations and models are consistent with all previous works.

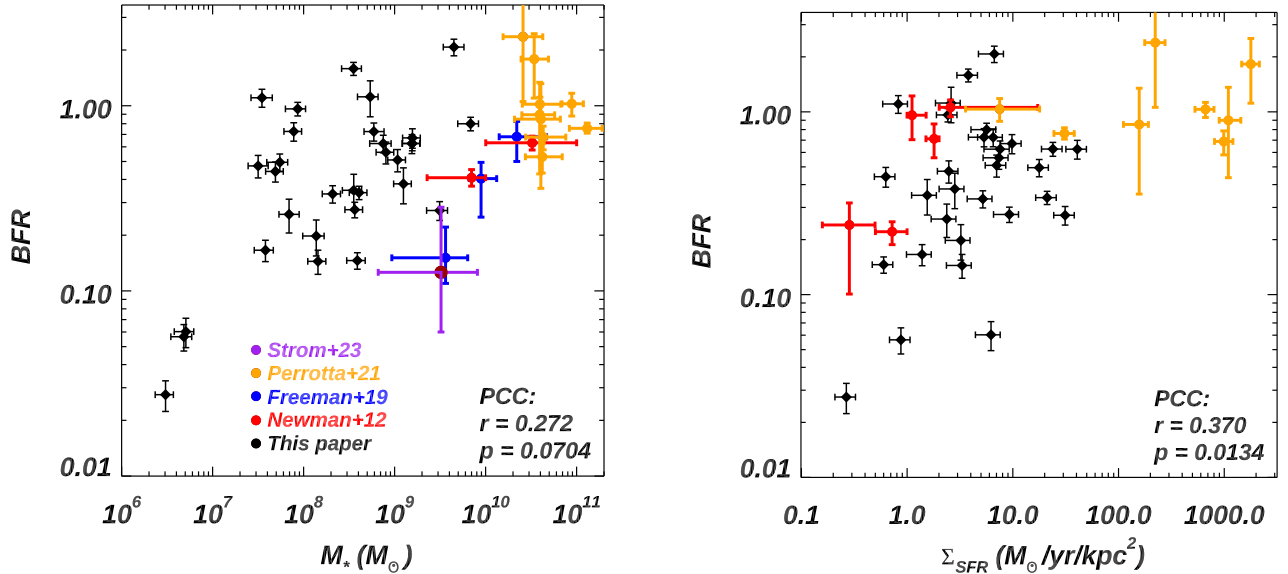


Figure 10. Comparisons of the broad flux ratio with galaxy stellar mass (**left**) and star-forming rate surface density (**right**). In each panel, galaxies in our sample are shown as black diamonds. We also present results from the literature as colored circles with crosses as the errorbars. These include the composite of 23 star-forming galaxies at $z = 2 - 3$ from JWST/CECILIA survey in purple (Strom et al. 2023), stacks of 27 star-forming galaxies at $z \sim 2$ from the SINS and zC-SINF surveys in red (N12), stacks of 113 galaxies at $z \sim 2$ from the MOSDEF survey in blue (F19), and 9 individual compact starburst galaxies at $z = 0.4 - 0.7$ from Perrotta et al. (2021) in orange. For the $z \sim 2$ samples, the detections of outflows in emission lines are mainly from massive galaxies due to the selection effects (i.e., hard to detect the broad components in lower SNRs spectra in dwarf galaxies). See discussion in Section 5.3.

5.3. Broad Flux Ratio

In this subsection, we discuss another important property of the emission line: the broad flux ratio (BFR), which is defined as the measured flux from the broad to narrow components. Note here we measure the flux of the whole broad or narrow components in contrast to measuring the flux of only the blueshifted component in Section 3.3. These choices are made to be consistent with previous studies of BFRs in the literatures (e.g., N12 and F19).

In the left panel of Figure 10, we compare BFR with the stellar mass (M_*) of the galaxy. Objects in our sample are shown as black diamonds. We also present various emission-line-based outflow detections from the literature, including stacks of 27 star-forming galaxies at $z \sim 2$ from the SINS and zC-SINF surveys in red (N12), stacks of 113 galaxies at $z \sim 2$ from the MOSDEF survey in blue (F19), 9 individual compact starburst galaxies at $z = 0.4 - 0.7$ from Perrotta et al. (2021) in orange, and the stack of 23 star-forming galaxies at $z = 2 - 3$ from JWST/CECILIA survey in purple (Strom et al. 2023). We note that like our analysis, all of these surveys adopt similar Gaussian fitting methods to extract the broad components from the emission lines. Most of the observations have similar spectral resolution ($R \sim 3000 - 5000$) for $H\alpha$ regions except that Strom et al. (2023) has

$R \sim 1000$, Perrotta et al. (2021) has $R \sim 2000$ and four of our galaxies have X-Shooter spectra with $R \sim 8800$. Thus, the major differences between galaxies should be their intrinsic properties (e.g., different M_* , SFR, and age) and redshifts.

Overall, there is a possible positive correlation ($\sim 1.7\sigma$) between BFR and M_* for all objects in the left panel of Figure 10, albeit with significant scatter. This trend was previously suggested in N12 and F19, but rejected by Perrotta et al. (2021). While all of the previous measurements have $M_* > 10^9 M_\odot$, the inclusion of low-mass SF galaxies from our sample shows that the trend likely extends below $10^8 M_\odot$. This correlation can be explained as the results of the stronger outflows powered by more massive galaxies. In addition, our galaxies show higher BFR at the same M_* compared with other samples. This is likely due to our selections of high SF systems (Section 2).

In the right panel of Figure 10, we compare the BFR with the surface brightness of SFR (Σ_{SFR}). N12 find this is the galaxy property that is best correlated with BFR (see red crosses for stacks from them), while Perrotta et al. (2021) suggest there is no clear correlation. When we consider all their measurements and our new data, we find all objects are consistent with a positive

correlation for $\Sigma_{\text{SFR}} < 100 \text{ M}_{\odot}/\text{yr}/\text{kpc}^2$, but reach a flat end beyond that.

Another instructive test is the effects of signal-to-noise⁷. F19 found that the measured BFR is dependent on SNR since it is hard to disentangle the broad and narrow components in low-SNR spectra. Thus, we show BFR versus SNR measured from the $\text{H}\alpha$ emission line in Figure 11. We find there is a tentative negative correlation ($\sim 2\sigma$), which has also been noticed in F19. We overlay individual galaxies from their MOSDEF sample with a broad component detection of $\sim 3\sigma$ significance as the blue symbols. While their galaxies typically have SNRs $\lesssim 100$, the measured BFRs are consistent with the low SNR end of our galaxies.

Furthermore, to test the impact of SNRs on BFR, we choose ten galaxies that match F19’s selection criteria of broad components ($\text{FWHM}^{\text{out}} > 275 \text{ km s}^{-1}$, marked in purple circles) and downgrade the observed spectra into SNR = 100, 50, and 20. Then we refit our galaxies using the method described in Section 3.2.2. For each galaxy, we find their spectra with SNR > 100 yield the same BFR within errorbars. When we reach SNR = 50, the extracted BFRs begin to have small to moderate fluctuations (0 – 50%). Finally, when we reach SNR = 20, we find most of the tested galaxies (8 out of 10) do not pass the F-test in spectral line fittings, i.e., one loses the information to isolate the broad components from emission lines (see Section 3.2). Thus, if the intrinsic emission lines in F19 are the same as ours, their detections of the broad, outflow components in the MOSDEF survey may be incomplete due to the limits of SNR in individual galaxy (average ~ 25 , Weldon et al. 2024). Overall, this test suggests that the accurate extractions of broad components from emission lines require SNR to be at least 50 and ideally larger than 100 for moderate resolution spectra ($R \sim 3000 - 5000$).

5.4. Implications for Future Galactic Outflow Studies

In the current work, we present how to jointly interpret the warm-ionized outflows seen from rest-UV absorption and optical emission lines for the same galaxy. These results can provide various implications for future studies of warm-ionized galactic outflows.

First of all, for warm ionized outflows, one could reliably predict the line kinematics of outflow absorption lines (e.g., Si II, Si IV) given the observed outflow emission lines (e.g., $\text{H}\alpha$, $\text{H}\beta$) and vice versa. This will be especially helpful when one of the outflow diagnos-

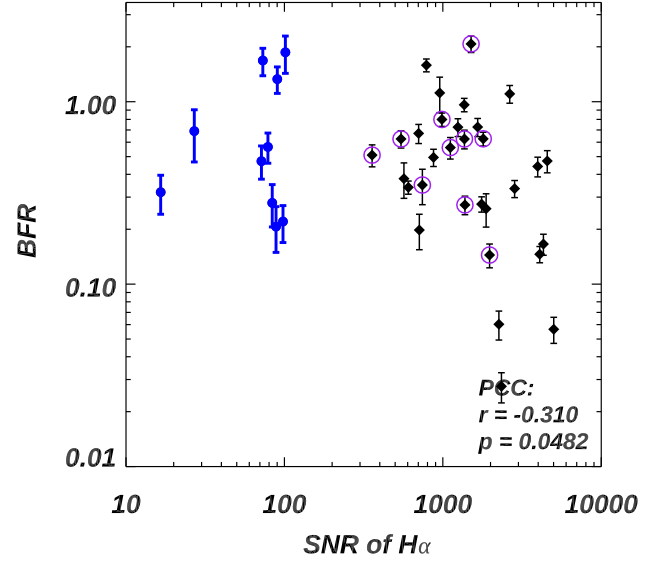


Figure 11. Comparisons of BFR and SNR measured from $\text{H}\alpha$ emission lines. Galaxies in our sample are shown in black diamonds, while individual $z \sim 2$ galaxies in Freeman et al. (2019) with $\sim 3\sigma$ significance detections of the broad components are shown as blue dots with 1σ errorbars. Our galaxies with $\text{H}\alpha$ broad component $\text{FWHM} > 275 \text{ km s}^{-1}$ are marked in purple circles, which match the selection criteria chosen by Freeman et al. (2019).

tics is not observed or difficult to access. For example, given the large samples of optically detected star-forming galaxies at low redshift, many show galactic outflow features in emission lines (e.g., $\sim 160,000$ from SDSS, Ciccone et al. 2016). However, only a very small portion have dedicated rest-UV coverage that allow us to study ionized outflow properties through absorption lines (e.g., ~ 100 from FUSE or HST/COS, Heckman et al. 2015; Xu et al. 2022a,b). On the other hand, for galaxies at $z \sim 2 - 4$, when the rest-UV spectra of galaxies can be directly accessed using large ground-based optical telescopes (e.g., from Keck and VLT, Steidel et al. 2014; Urrutia et al. 2019), their rest-optical spectral ranges can be inaccessible from the ground⁸ and JWST observations are expensive. Thus, our current work can provide guidelines for 1) designing future spectroscopic surveys by making realistic predictions of one type of outflow diagnostics using another, and 2) making fair comparisons of outflow properties across the cosmic times using different diagnostics.

Furthermore, our work indicates that models and simulations of galactic outflows can now have additional

⁷ Hereafter, the SNR of a spectral line is defined as its fitted flux divided by the error of the flux. This is to be consistent with the definition in F19.

⁸ Due to telluric absorption of Earth’s atmosphere or limited spectral coverage of ground-based spectrographs.

constraints by matching outflow features from both absorption and emission lines for the same galaxy. This can effectively double the number of constraints and could potentially break degeneracy of many models that have been adopted to explain one of the outflow diagnostics (e.g., Cottle et al. 2018; de la Cruz et al. 2021; Li et al. 2024; Huberty et al. 2024). We have plans to study more sophisticated models in future papers, e.g., using SALT (Carr et al. 2023), to vary the density and velocity distributions to fit the observed absorption and emission lines for each galaxy.

Finally, our work has a few caveats or limitations: 1) The current sample is not large. While we find a tight correlation in kinematics of the two outflow diagnostics, we do not have enough objects to reveal a clear correlation in outflow density and rates. 2) Outflow properties are spatially dependent. Our LOS integrated observations missed the spatial variations, which can provide additional constraints on the interpretation and models of galactic outflows. Thus, future integral field unit (IFU) observations covering both rest-UV and rest-optical spectral regions of the same galaxy will provide useful insights toward this direction. 3) Galaxies and their outflows evolve over cosmic times. Our work only focuses on SF galaxies at low-redshift. Similar analyses should also be conducted for large samples of SF galaxies at the cosmic noon and in the early universe.

6. CONCLUSION

In this paper, we shine a light on the connection between galactic outflow properties measured from two different diagnostics, i.e., rest-UV absorption and rest-optical emission lines. We have collected a sample of 33 low-redshift SF galaxies that cover a wide range of stellar mass, star-formation rate, and metallicity. For each galaxy, we combine their UV observations from HST/COS and optical observations from Keck/ESI or VLT/X-Shooter. We adopt multiple Gaussian profiles to fit the observed emission and absorption lines and isolate the outflow components. Then, we compare the properties of the two sets of outflow diagnostics in various ways. The principal results are as follows:

1. For all galaxies with an outflow component detected in its absorption lines, we also detect it in its emission lines.
2. The maximum outflow velocity (or line width) derived from the emission and absorption lines are tightly correlated. On average, outflows detected in emission lines reach $\sim 56\%$ of the maximum velocity and 60% of the line widths than those of absorption lines for the same galaxy.

3. Outflow sizes are also tightly correlated when measured from emission and absorption lines. Outflows seen in emission lines are always detected in inner regions to the center of the galaxy and possibly have higher gas densities than those of absorption lines detected in the same galaxy.

4. We constructed analytical galactic wind models giving M 82 velocity and density profiles. We find the spherical outflow models with a density distribution $\propto r^{-2.0}$ on-average matches the observed correlations well. Bi-conical outflow models from SALT shows that the outflow geometry can affect the observed line profiles but predictions are still consistent with the observed correlations.

5. By comparing with previous studies, we find that our reported correlations of the two outflow diagnostics are consistent with observations in the literature. However, we are the first to analyze the correlations and attempt to quantitatively understand them along with models.

6. We study the broad-flux-ratios (BFRs) of our galaxies and compare them with various other outflow studies. We find there are possible correlations between BFR and galaxy stellar mass and with SFR surface density. We also find that signal-to-noise larger than 50 is required to accurately extract BFR from emission lines with spectral resolution ~ 3000 .

7. We also highlight a few implications for future studies. Given the correlations found between the two diagnostics, one can now reliably predict the line kinematics of outflow absorption lines, given the observed outflow emission lines, and vice versa. This should help design future spectroscopic surveys and make comparisons between heterogeneous outflow samples. Furthermore, our work indicates that future models and simulations can now have additional constraints by considering both outflow absorption and emission lines for the same galaxy.

1 X.X. and A.H. acknowledge supports from NASA STScI
 2 grant HST-AR-17042. X.X. thank T. Thompson for
 3 helpful discussions. X.X., A.H., and T.J. thank M.
 4 Rafelski and R. Sanders for Keck/ESI observations and
 5 data reductions. X.X thank Keerthi Vasan G. C. for
 6 useful comments.

7 This research is based on observations made with the
 8 NASA/ESA Hubble Space Telescope obtained from the
 9 Space Telescope Science Institute, which is operated by
 10 the Association of Universities for Research in Astron-
 11 omy, Inc., under NASA contract NAS 5-26555. These
 12 observations are associated with programs 11727, 12928,
 13 13017, 13293, 14080, 14168, 14679, 15185, 15626, 15646,
 14 15099, 15840, 16643, and 17526.

15 Part of the data presented herein were obtained at
 16 Keck Observatory, which is a private 501(c)3 non-profit
 17 organization operated as a scientific partnership among
 18 the California Institute of Technology, the University
 19 of California, and the National Aeronautics and Space
 20 Administration. The Observatory was made possible by
 21 the generous financial support of the W. M. Keck Foun-
 22 dation. The authors wish to recognize and acknowledge
 23 the very significant cultural role and reverence that the
 24 summit of Maunakea has always had within the Na-
 25 tive Hawaiian community. We are most fortunate to
 26 have the opportunity to conduct observations from this
 27 mountain.

28 Part of the data presented were collected from the
 29 European Southern Observatory under ESO programs
 30 085.B-0784(A) and 096.B-0192(A).

31 Additional data analyses were done using Interactive
 32 Data Language (IDL), version 8.7.3, L3Harris Geospa-
 33 tial, Boulder, Colorado, USA.

Facilities: HST (COS), Keck (ESI), VLT (X-
 Shooter)

Software: astropy (Astropy Collaboration et al.
 2022), CLOUDY (Ferland et al. 2017), jupyter (Kluyver
 et al. 2016), MPFIT (Markwardt 2009) , ESIRedux
 (Prochaska et al. 2007),

APPENDIX

A. SPECTRA LINE FITTING FOR ALL GALAXIES

We show fits to UV-absorption and optical-emission lines for all galaxies in our sample in Figures 12 to 16.

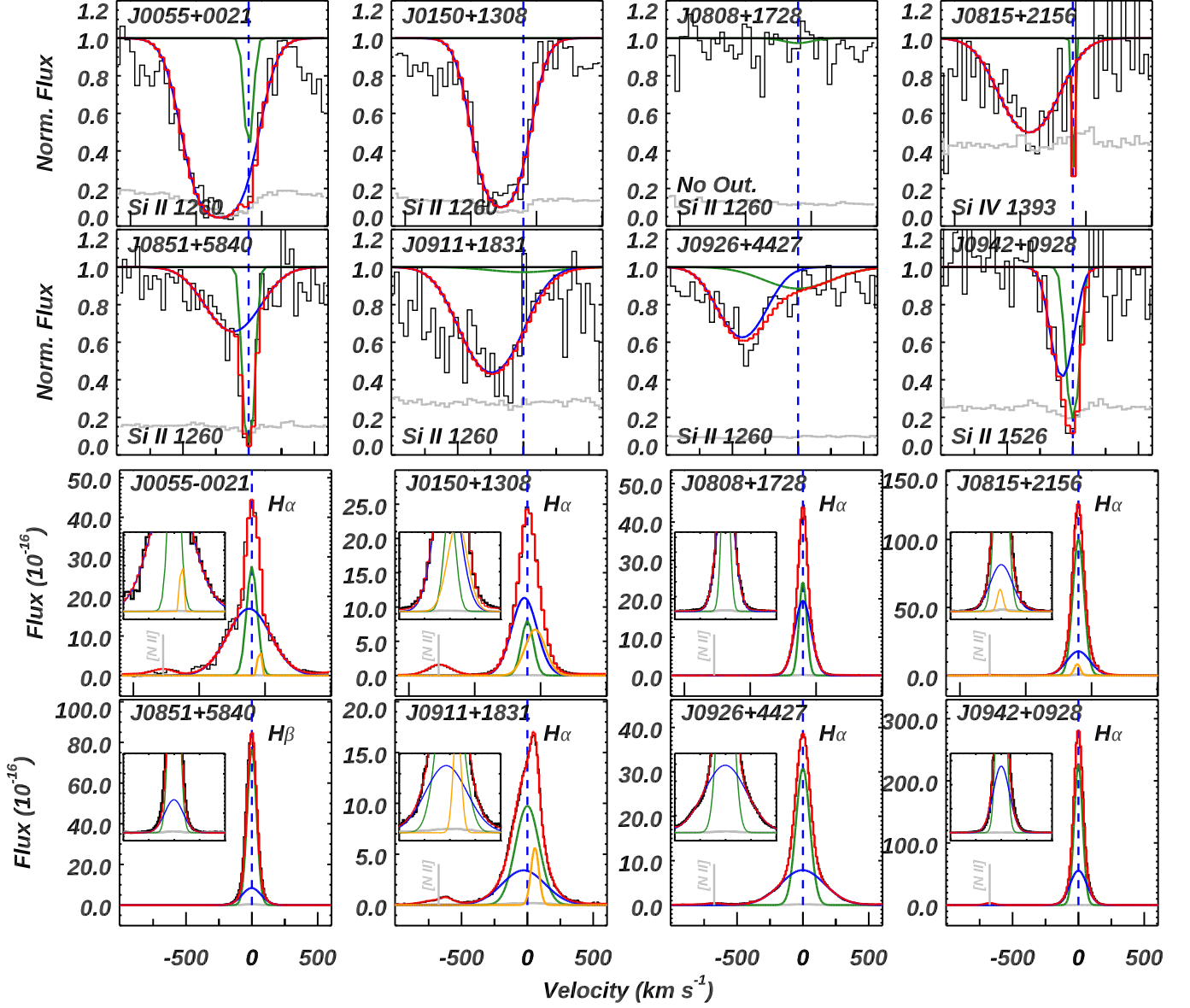


Figure 12. Spectral line fitting to for galaxies in our sample. **Top two** and **bottom two** rows are for UV-absorption and optical-emission lines, respectively, for the same 8 galaxies. For UV spectra, we show Si II $\lambda 1260$ absorption line unless it is not covered or contaminated. Similarly, for optical spectra, we mainly show the strong lines from H α or H β . The data and errors are shown in black and gray histograms. We adopt double- to triple-Gaussian profiles to fit the lines. The static ISM and outflow components are shown in green and blue, respectively. For emission lines, the third Gaussian (when necessary) is shown in orange. The red line is the summation of all models. For lines with no outflow signatures, we show only the static ISM component in green and mark it as “No Out.”. The inset shows a zoom-in view of the broad wings in the emission line. We indicate the locations of Galactic absorption in vertical gray dashed lines and [N II] $\lambda 6548$ in vertical gray solid lines. See detailed discussion of the fittings in Section 3.2.

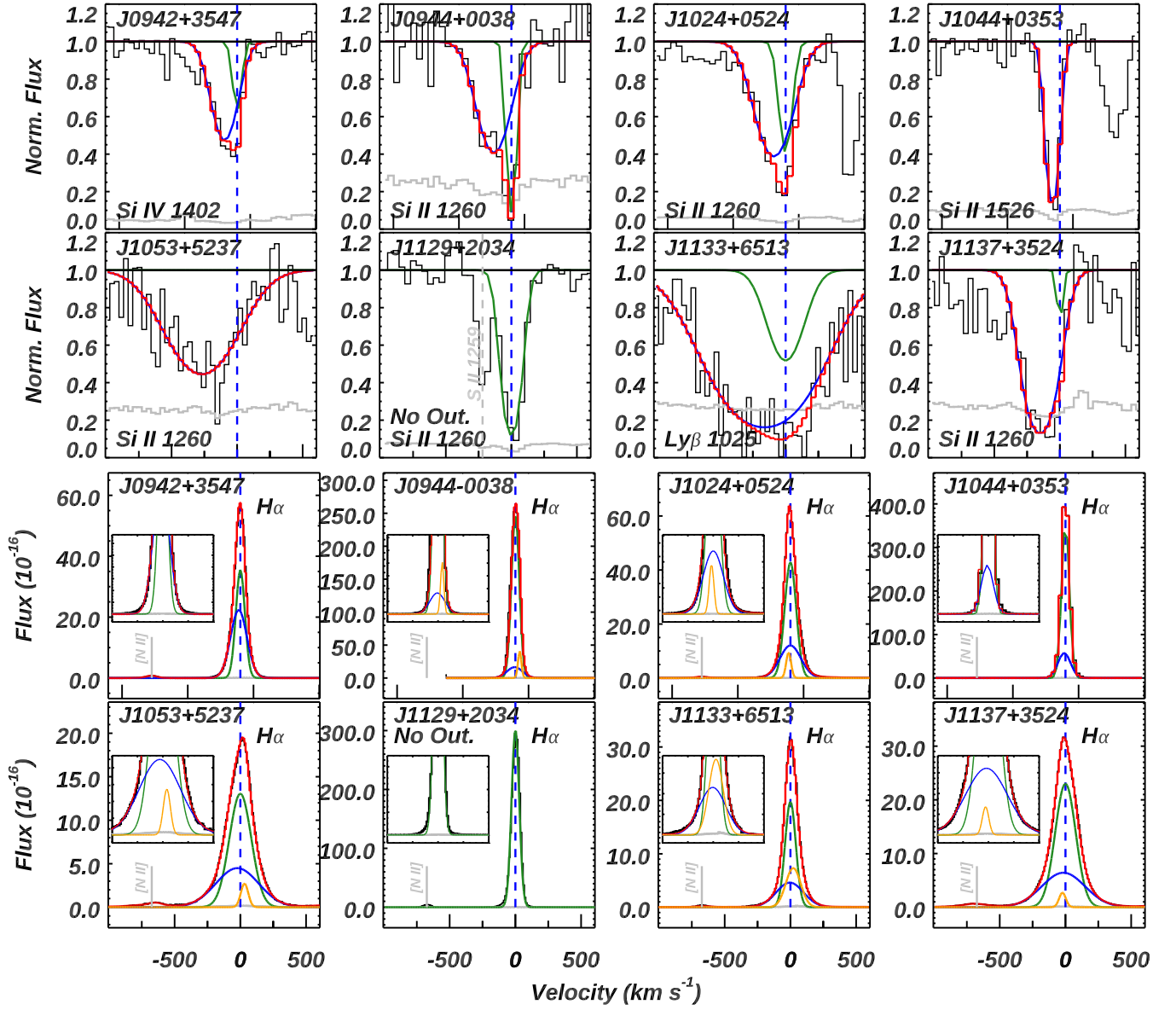


Figure 13. Same as Figure 12 for the other 8 galaxies in our sample.

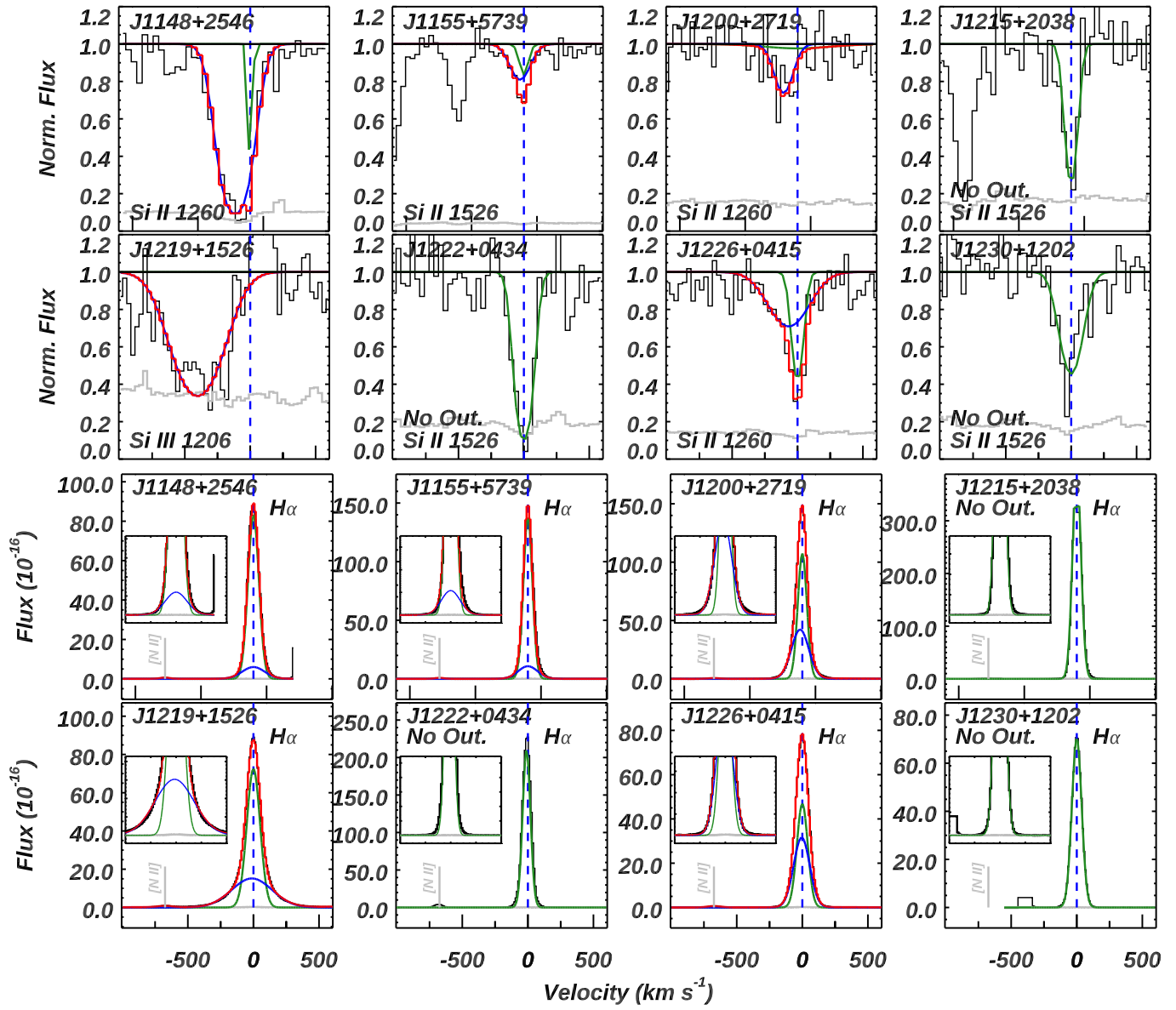


Figure 14. Same as Figure 12 for the other 8 galaxies in our sample. J1148+2546 has a gap at the right side of H α , but it does not affect our line fit here.

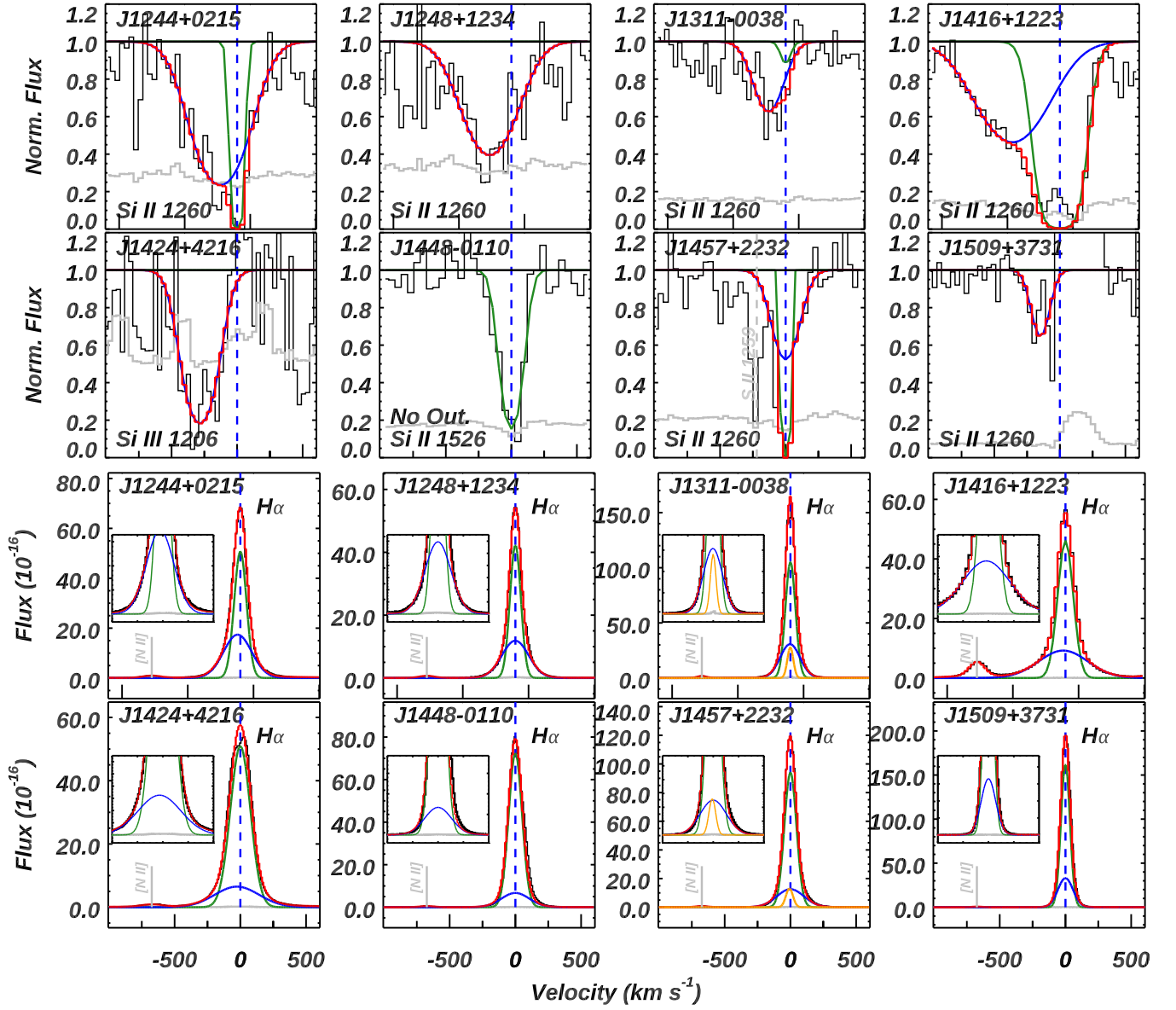


Figure 15. Same as Figure 12 for the other 8 galaxies in our sample.

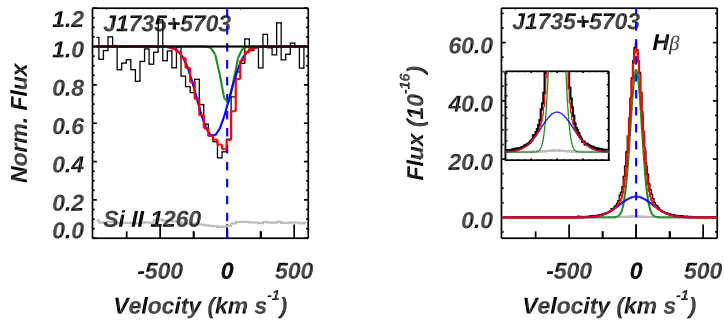


Figure 16. Same as Figure 12 for the last object in our sample.

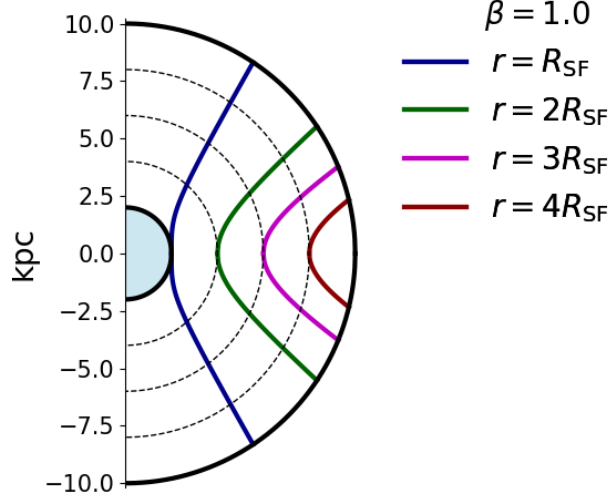


Figure 17. Various intersections (i.e., Γ) of the surface at constant observed velocity in the outflow with the plane perpendicular to the plane of the sky. We also adopt the $\beta = 1$ velocity field as specified in Equation 8.

B. SALT MODELS OF BI-CONICAL GALACTIC OUTFLOWS IN ABSORPTION AND EMISSION LINES

In Semi-analytical Line Transfer (SALT) model, we begin by computing the surfaces of constant observed velocity in the outflow, given the velocity distribution defined by Equation 8. Following Carr et al. (2023), it is sufficient to only consider the curve defined by the intersection of the surface with the plane perpendicular to the plane of the sky, i.e., we have:

$$\Gamma(s, \xi) = \left(\frac{x}{y} \frac{1}{1-y^{1/\beta}}, \left[\left(\frac{1}{1-y^{1/\beta}} \right)^2 - \left(\frac{1}{1-y^{1/\beta}} \right)^2 \frac{x^2}{y^2} \right]^{1/2} \right), \quad (\text{B1})$$

where $y = v/v_\infty$ and $x = v_{\text{obs}}/v_\infty$. We compute several curves for a spherical outflow in Figure 17 for $\beta = 1.0$. The velocity field behaves similarly to a power law with index less than one (see the appendix of Carr et al. 2018).

Next, we compute the Sobolev optical depth (Castor 1970; Lamers & Cassinelli 1999) from Equation 18 in Carr et al. (2023). Keeping the same form for the density field as Equation 9, $n = n_0 (r/R_{\text{SF}})^\gamma$, we have

$$\tau_S = \tau_0 \frac{(1 - y^{(1/\beta)})^{\gamma-1} y^{-1}}{1 + [\beta y^{-1/\beta} - (\beta + 1)] \left(\frac{x}{y} \right)^2}, \quad (\text{B2})$$

where

$$\tau_0 = \frac{\pi e^2}{m_e c} f \lambda \frac{R_{\text{SF}}}{v_\infty} n_0. \quad (\text{B3})$$

We can now calculate the absorption profile resulting from the removal of photons by the surfaces of constant observed velocity. Adapting Equation 7 in Carr et al. (2023), we have the normalized intensity of absorption lines as:

$$\frac{I_{\text{abs}}}{I_0} = \frac{F_\lambda}{F_{c,\lambda}} - \frac{F_\lambda}{F_{c,\lambda}} \int_x^{y_1} 2 \frac{x^2 \beta - y^{1/\beta} (x^2 (\beta + 1) + y^2)}{\beta y^3 (y^{1/\beta} - 1)^3} \times (1 - e^{-\tau_S}) dy \quad (\text{B4})$$

where y_1 represents the maximum radial velocity a shell can have and still contribute to continuum absorption. It can be obtained from the relation:

$$x^2 = y_1^2 - y_1^2 (1 - y_1^{1/\beta})^2. \quad (\text{B5})$$

In a similar fashion, we can compute the emission component by adapting Equations 16 and 17 from Carr et al. (2023). We have

$$\frac{I_{\text{em,blue}}}{I_0} = \int_x^1 f_g \frac{dy}{2y} \int_{y \cos \Theta_c}^y \frac{F(x')}{F_c(x)} \frac{2}{\beta} \left[\frac{x'^2 \beta - y^{1/\beta} (x'^2 (\beta + 1) + y^2)}{\beta y^3 (y^{1/\beta} - 1)^3} \right] (1 - e^{-\tau}) dx',$$

and

$$\frac{I_{\text{em,red}}}{I_0} = \int_{y_1}^1 f_g \frac{dy}{2y} \int_{y \cos \Theta_c}^y \frac{F(x')}{F_c(x)} \frac{2}{\beta} \left[\frac{x'^2 \beta - y^{1/\beta} (x'^2 (\beta + 1) + y^2)}{\beta y^3 (y^{1/\beta} - 1)^3} \right] (1 - e^{-\tau}) dx',$$

where

$$\Theta_C = \arcsin([1 - y^{1/\beta}]^{-1}) \quad (\text{B6})$$

is the angle subtended by a shell of intrinsic velocity y along the continuum. Note that we have included the geometric scale factor, f_g , from Equation 21 in Carr et al. (2023), which accounts for the geometry of the bi-cone and can be adapted to the new velocity field in the obvious way.

Next, we develop an emission component emanating from the bi-cone e.g., Scuderi et al. 1992. It will be convenient, however, to first solve for the case of a spherical outflow and later scale to the profile of a bi-cone using f_g . We assume an electron density field in the form of:

$$n_e = n_{0,e} \left(\frac{R_{\text{SF}}}{r} \right)^\epsilon, \quad (\text{B7})$$

where $n_{0,e}$ is the density of electrons at R_{SF} and ϵ is the power law index. In our calculations, we take $\epsilon = \gamma$ as in Equation 9, but we keep them in different letters in the following equations for interpretation purpose.

At a temperature around 10^4 K the contribution to the intrinsic H α emission will be dominated by recombination. Thus, we compute the intrinsic luminosity of H α emission from a spherical shell of radius, r , and thickness, dr , as

$$L_{\text{shell}} = h\nu n_e n_{\text{H}^0} q_{\text{rec}}^{\text{H}\alpha} 4\pi r^2 dr, \quad (\text{B8})$$

where h is Plank's constant and $q_{\text{rec}}^{\text{H}\alpha}$ is the H α recombination coefficient. Plugging in the definitions of the various density fields and rewriting the expression in terms of the y , we have

$$L_{\text{shell}} = \frac{4\pi h\nu n_{e,0} n_{\text{H}^0,0} q_{\text{rec}}^{\text{H}\alpha} R_{\text{SF}}^3}{\beta} \left(1 - y^{1/\beta}\right)^{\gamma+\epsilon-4} y^{\frac{1-\beta}{\beta}} dy. \quad (\text{B9})$$

To compute the resulting line profile in terms of the observed velocities, v_{obs} , we use the same emission band contour theory developed by Beals (1931) and used by Carr et al. (2018, 2023). In this context, the flux, dF_{BC} , emitted by an arbitrary band contour on the shell (see Figure 4 from Carr et al. 2018) becomes

$$dF_{BC} = L_{\text{shell}} \frac{dv_{\text{obs}}}{4\pi r_\infty^2 2v}, \quad (\text{B10})$$

where r_∞ is the distance from the shell to the observer and v is the radial velocity of the shell. Writing this expression in terms of y and integrating over the shell, we compute the normalized blue emission profile for a bi-conical outflow as

$$\frac{F_{\text{int.em.,blue}}}{F_0} = \int_x^1 f_g \frac{h\nu n_{e,0} n_{\text{H}^0,0} q_{\text{rec}}^{\text{H}\alpha} R_{\text{SF}}^3}{F_c 2\beta r_\infty^2} \left(1 - y^{1/\beta}\right)^{\gamma+\epsilon-4} y^{\frac{1-\beta}{\beta}} dy \quad (\text{B11})$$

and the normalized red emission profile as

$$\frac{F_{\text{int.em.,red}}}{F_0} = \int_{y_1}^1 f_g \frac{h\nu n_{e,0} n_{\text{H}^0,0} q_{\text{rec}}^{\text{H}\alpha} R_{\text{SF}}^3}{F_c 2\beta r_\infty^2} \left(1 - y^{1/\beta}\right)^{\gamma+\epsilon-4} y^{\frac{1-\beta}{\beta}} dy \quad (\text{B12})$$

Note that, once again, we scale by f_g to collapse the solution for a spherical outflow to that of a bi-cone. The results of these profiles given M 82 parameters are shown in Figures 8.

Table 3. Other Measurements for Galaxies in our Sample

ID	Log M_{\star} (M_{\odot})	Log SFR ($M_{\odot} \text{ yr}^{-1}$)	Emi. Log R^{out} (kpc)	Abs. Log R^{out} (kpc)	$E(B - V)_{\text{int.}}$
J0055-0021	$9.7^{+0.1}_{-0.1}$	$1.1^{+0.1}_{-0.1}$	< -0.2	$0.6^{+0.2}_{-0.2}$	0.089
J0150+1308	$8.7^{+0.1}_{-0.1}$	$0.8^{+0.1}_{-0.1}$	$0.2^{+0.07}_{-0.08}$	$0.7^{+0.2}_{-0.2}$	0.190
J0808+1728	$8.5^{+0.1}_{-0.1}$	$-0.5^{+0.1}_{-0.1}$	< -0.4	$0.04^{+0.01}_{-0.01}$	0.000
J0815+2156	$8.6^{+0.3}_{-0.2}$	$1.2^{+0.1}_{-0.1}$	$-0.2^{+0.09}_{-0.1}$	$0.5^{+0.1}_{-0.1}$	0.187
J0851+5840	$8.1^{+0.2}_{-0.1}$	$0.7^{+0.1}_{-0.1}$	$-0.2^{+0.08}_{-0.10}$	$0.6^{+0.2}_{-0.2}$	0.001
J0911+1831	$9.0^{+0.1}_{-0.2}$	$1.2^{+0.1}_{-0.1}$	$0.3^{+0.07}_{-0.09}$	$0.7^{+0.2}_{-0.2}$	0.094
J0926+4427	$9.8^{+0.2}_{-0.1}$	$1.2^{+0.4}_{-0.1}$	$0.009^{+0.06}_{-0.07}$	$0.7^{+0.2}_{-0.2}$	0.230
J0942+3547	$7.5^{+0.1}_{-0.1}$	$-1.4^{+0.1}_{-0.1}$	$-0.2^{+0.06}_{-0.07}$	$-0.02^{+0.007}_{-0.007}$	0.038
J0942+0928	$7.5^{+0.1}_{-0.1}$	$-0.8^{+0.1}_{-0.1}$	$-0.8^{+0.07}_{-0.08}$	> 0.01	0.253
J0944-0038	$6.7^{+0.2}_{-0.1}$	$-1.9^{+0.1}_{-0.1}$	$-0.7^{+0.06}_{-0.07}$	> -0.2	0.000
J1024+0524	$7.7^{+0.1}_{-0.2}$	$-0.6^{+0.2}_{-0.3}$	$-0.1^{+0.06}_{-0.07}$	$0.4^{+0.1}_{-0.1}$	0.054
J1044+0353	$7.8^{+0.1}_{-0.1}$	$-0.8^{+0.1}_{-0.1}$	< -1.1	$0.004^{+0.001}_{-0.001}$	0.000
J1053+5237	$8.9^{+0.1}_{-0.1}$	$1.4^{+0.3}_{-0.1}$	$-0.3^{+0.2}_{-0.2}$	$0.7^{+0.2}_{-0.2}$	0.213
J1129+2034	$6.7^{+0.2}_{-0.1}$	$-1.3^{+0.1}_{-0.1}$...	$-0.3^{+0.1}_{-0.1}$	0.586
J1133+6513	$9.1^{+0.2}_{-0.2}$	$1.1^{+0.1}_{-0.1}$	$0.3^{+0.07}_{-0.09}$	$0.8^{+0.2}_{-0.2}$	0.065
J1137+3524	$8.9^{+0.2}_{-0.2}$	$1.3^{+0.4}_{-0.1}$	$0.2^{+0.07}_{-0.09}$	$0.7^{+0.2}_{-0.2}$	0.199
J1148+2546	$8.6^{+0.1}_{-0.1}$	$-0.2^{+0.1}_{-0.1}$	$-0.2^{+0.07}_{-0.08}$	> 0.5	0.000
J1155+5739	$7.6^{+0.1}_{-0.1}$	$-0.9^{+0.1}_{-0.1}$	$-0.3^{+0.06}_{-0.07}$	$0.06^{+0.02}_{-0.02}$	0.001
J1200+2719	$7.9^{+0.1}_{-0.2}$	$0.7^{+0.1}_{-0.1}$	$-0.2^{+0.08}_{-0.1}$	$0.5^{+0.1}_{-0.1}$	0.133
J1215+2038	$5.9^{+0.2}_{-0.1}$	$-2.2^{+0.1}_{-0.1}$...	$-0.5^{+0.2}_{-0.2}$	0.000
J1219+1526	$9.2^{+0.2}_{-0.2}$	$1.6^{+0.1}_{-0.1}$	$-0.1^{+0.06}_{-0.07}$	$0.5^{+0.1}_{-0.1}$	0.214
J1222+0434	$5.3^{+0.1}_{-0.1}$	$-1.8^{+0.1}_{-0.1}$...	> -0.3	0.191
J1226+0415	$7.9^{+0.1}_{-0.1}$	$0.5^{+0.2}_{-0.3}$	$-0.1^{+0.08}_{-0.09}$	$0.5^{+0.2}_{-0.2}$	0.000
J1230+1202	$6.5^{+0.1}_{-0.1}$	$-2.5^{+0.1}_{-0.1}$...	> -0.3	0.000
J1244+0215	$8.8^{+0.1}_{-0.2}$	$1.7^{+0.4}_{-0.1}$	$0.006^{+0.10}_{-0.1}$	$0.9^{+0.3}_{-0.3}$	0.275
J1248+1234	$9.2^{+0.3}_{-0.2}$	$1.5^{+0.3}_{-0.2}$	$0.05^{+0.06}_{-0.07}$	$0.7^{+0.2}_{-0.2}$	0.110
J1311-0038	$7.7^{+0.1}_{-0.1}$	$0.8^{+0.1}_{-0.1}$	$-0.5^{+0.06}_{-0.07}$	$0.3^{+0.09}_{-0.09}$	0.191
J1416+1223	$9.2^{+0.5}_{-0.2}$	$1.1^{+0.1}_{-0.1}$	< -0.2	$0.4^{+0.1}_{-0.1}$	0.306
J1424+4216	$9.5^{+0.1}_{-0.1}$	$1.4^{+0.1}_{-0.1}$	< -0.07	$0.5^{+0.1}_{-0.1}$	0.194
J1448-0110	$8.2^{+0.1}_{-0.1}$	$-0.5^{+0.1}_{-0.1}$	$-0.4^{+0.07}_{-0.08}$	$0.09^{+0.03}_{-0.03}$	0.129
J1457+2232	$8.6^{+0.1}_{-0.2}$	$1.2^{+0.1}_{-0.1}$	$-0.1^{+0.09}_{-0.1}$	$0.6^{+0.2}_{-0.2}$	0.080
J1509+3731	$8.3^{+0.1}_{-0.1}$	$-0.2^{+0.1}_{-0.1}$	$-0.2^{+0.07}_{-0.08}$	$0.1^{+0.04}_{-0.04}$	0.093
J1735+5703	$8.6^{+0.1}_{-0.1}$	$0.07^{+0.1}_{-0.1}$	$-0.5^{+0.09}_{-0.1}$	$0.5^{+0.1}_{-0.1}$	0.001

Note. –

(1) From left to right, we list the estimated stellar mass (Section 3.1), star-forming rate (Section 3.4), outflow sizes (R^{out}) measured from emission lines (Section 4.3), R^{out} measured from absorption lines (Section 4.3), and intrinsic dust extinction (Section 3.4) for each galaxy.

C. ADDITIONAL MEASURED PARAMETERS

We summarize other measurements for each galaxy in Table 3.

REFERENCES

- Amorín, R. O., Rodríguez-Henríquez, M., Fernández, V., et al. 2024, arXiv e-prints, arXiv:2401.04278, doi: 10.48550/arXiv.2401.04278
- Astropy Collaboration, Price-Whelan, A. M., Lim, P. L., et al. 2022, ApJ, 935, 167, doi: 10.3847/1538-4357/ac7c74

- Avery, C. R., Wuyts, S., Förster Schreiber, N. M., et al. 2022, *MNRAS*, 511, 4223, doi: [10.1093/mnras/stac190](https://doi.org/10.1093/mnras/stac190)
- Beals, C. S. 1931, *MNRAS*, 91, 966, doi: [10.1093/mnras/91.9.966](https://doi.org/10.1093/mnras/91.9.966)
- Berg, D. A., James, B. L., King, T., et al. 2022, arXiv e-prints, arXiv:2203.07357. <https://arxiv.org/abs/2203.07357>
- Burchett, J. N., Rubin, K. H. R., Prochaska, J. X., et al. 2021, *ApJ*, 909, 151, doi: [10.3847/1538-4357/abd4e0](https://doi.org/10.3847/1538-4357/abd4e0)
- Carniani, S., Venturi, G., Parlanti, E., et al. 2024, *A&A*, 685, A99, doi: [10.1051/0004-6361/202347230](https://doi.org/10.1051/0004-6361/202347230)
- Carr, C., Michel-Dansac, L., Blaizot, J., et al. 2023, *ApJ*, 952, 88, doi: [10.3847/1538-4357/acd331](https://doi.org/10.3847/1538-4357/acd331)
- Carr, C., Scarlata, C., Henry, A., & Panagia, N. 2021, *ApJ*, 906, 104, doi: [10.3847/1538-4357/abc7c3](https://doi.org/10.3847/1538-4357/abc7c3)
- Carr, C., Scarlata, C., Panagia, N., & Henry, A. 2018, *ApJ*, 860, 143, doi: [10.3847/1538-4357/aac48e](https://doi.org/10.3847/1538-4357/aac48e)
- Castor, J. I. 1970, *MNRAS*, 149, 111, doi: [10.1093/mnras/149.2.111](https://doi.org/10.1093/mnras/149.2.111)
- Chang, Y.-Y., van der Wel, A., da Cunha, E., & Rix, H.-W. 2015, *ApJS*, 219, 8, doi: [10.1088/0067-0049/219/1/8](https://doi.org/10.1088/0067-0049/219/1/8)
- Chisholm, J., Rigby, J. R., Bayliss, M., et al. 2019, *ApJ*, 882, 182, doi: [10.3847/1538-4357/ab3104](https://doi.org/10.3847/1538-4357/ab3104)
- Chisholm, J., Tremonti, C., & Leitherer, C. 2018, *MNRAS*, 481, 1690, doi: [10.1093/mnras/sty2380](https://doi.org/10.1093/mnras/sty2380)
- Chisholm, J., Tremonti, C. A., Leitherer, C., & Chen, Y. 2017, *MNRAS*, 469, 4831, doi: [10.1093/mnras/stx1164](https://doi.org/10.1093/mnras/stx1164)
- Chisholm, J., Tremonti, C. A., Leitherer, C., Chen, Y., & Wofford, A. 2016a, *MNRAS*, 457, 3133, doi: [10.1093/mnras/stw178](https://doi.org/10.1093/mnras/stw178)
- Chisholm, J., Tremonti, Christy, A., Leitherer, C., & Chen, Y. 2016b, *MNRAS*, 463, 541, doi: [10.1093/mnras/stw1951](https://doi.org/10.1093/mnras/stw1951)
- Choi, J., Dotter, A., Conroy, C., et al. 2016, *ApJ*, 823, 102, doi: [10.3847/0004-637X/823/2/102](https://doi.org/10.3847/0004-637X/823/2/102)
- Cicone, C., Maiolino, R., & Marconi, A. 2016, *A&A*, 588, A41, doi: [10.1051/0004-6361/201424514](https://doi.org/10.1051/0004-6361/201424514)
- Conroy, C., Naidu, R. P., Zaritsky, D., et al. 2019, *ApJ*, 887, 237, doi: [10.3847/1538-4357/ab5710](https://doi.org/10.3847/1538-4357/ab5710)
- Cottle, J. N., Scannapieco, E., & Brügggen, M. 2018, *ApJ*, 864, 96, doi: [10.3847/1538-4357/aad55c](https://doi.org/10.3847/1538-4357/aad55c)
- Davies, R. L., Förster Schreiber, N. M., Übler, H., et al. 2019, *ApJ*, 873, 122, doi: [10.3847/1538-4357/ab06f1](https://doi.org/10.3847/1538-4357/ab06f1)
- Davis, J. D., Tremonti, C. A., Swiggum, C. N., et al. 2023, *ApJ*, 951, 105, doi: [10.3847/1538-4357/acbbbf](https://doi.org/10.3847/1538-4357/acbbbf)
- de la Cruz, L. M., Schneider, E. E., & Ostriker, E. C. 2021, *ApJ*, 919, 112, doi: [10.3847/1538-4357/ac04ac](https://doi.org/10.3847/1538-4357/ac04ac)
- Draine, B. T., & Li, A. 2007, *ApJ*, 657, 810, doi: [10.1086/511055](https://doi.org/10.1086/511055)
- Ferland, G. J., Chatzikos, M., Guzmán, F., et al. 2017, *RMxAA*, 53, 385. <https://arxiv.org/abs/1705.10877>
- Fisher, D. B., Bolatto, A. D., Chisholm, J., et al. 2024, arXiv e-prints, arXiv:2405.03686, doi: [10.48550/arXiv.2405.03686](https://doi.org/10.48550/arXiv.2405.03686)
- Flury, S. R., Jaskot, A. E., Ferguson, H. C., et al. 2022a, *ApJS*, 260, 1, doi: [10.3847/1538-4365/ac5331](https://doi.org/10.3847/1538-4365/ac5331)
- . 2022b, *ApJ*, 930, 126, doi: [10.3847/1538-4357/ac61e4](https://doi.org/10.3847/1538-4357/ac61e4)
- Freeman, W. R., Siana, B., Kriek, M., et al. 2019, *ApJ*, 873, 102, doi: [10.3847/1538-4357/ab0655](https://doi.org/10.3847/1538-4357/ab0655)
- Genzel, R., Newman, S., Jones, T., et al. 2011, *ApJ*, 733, 101, doi: [10.1088/0004-637X/733/2/101](https://doi.org/10.1088/0004-637X/733/2/101)
- Grimes, J. P., Heckman, T., Aloisi, A., et al. 2009, *ApJS*, 181, 272, doi: [10.1088/0067-0049/181/1/272](https://doi.org/10.1088/0067-0049/181/1/272)
- Guo, Y., Bacon, R., Bouché, N. F., et al. 2023, *Nature*, 624, 53, doi: [10.1038/s41586-023-06718-w](https://doi.org/10.1038/s41586-023-06718-w)
- Heckman, T. M., Alexandroff, R. M., Borthakur, S., Overzier, R., & Leitherer, C. 2015, *ApJ*, 809, 147, doi: [10.1088/0004-637X/809/2/147](https://doi.org/10.1088/0004-637X/809/2/147)
- Heckman, T. M., & Best, P. N. 2023, arXiv e-prints, arXiv:2301.11960, doi: [10.48550/arXiv.2301.11960](https://doi.org/10.48550/arXiv.2301.11960)
- Heckman, T. M., Lehnert, M. D., Strickland, D. K., & Armus, L. 2000, *ApJS*, 129, 493, doi: [10.1086/313421](https://doi.org/10.1086/313421)
- Henry, A., Scarlata, C., Martin, C. L., & Erb, D. 2015, *ApJ*, 809, 19, doi: [10.1088/0004-637X/809/1/19](https://doi.org/10.1088/0004-637X/809/1/19)
- Huberty, M., Carr, C., Scarlata, C., et al. 2024, arXiv e-prints, arXiv:2406.03646, doi: [10.48550/arXiv.2406.03646](https://doi.org/10.48550/arXiv.2406.03646)
- James, B. L., Berg, D. A., King, T., et al. 2022, *ApJ*
- Jaskot, A. E., & Oey, M. S. 2014, *ApJL*, 791, L19, doi: [10.1088/2041-8205/791/2/L19](https://doi.org/10.1088/2041-8205/791/2/L19)
- Jaskot, A. E., Oey, M. S., Scarlata, C., & Dowd, T. 2017, *ApJL*, 851, L9, doi: [10.3847/2041-8213/aa9d83](https://doi.org/10.3847/2041-8213/aa9d83)
- Johnson, B. D., Leja, J., Conroy, C., & Speagle, J. S. 2021, *ApJS*, 254, 22, doi: [10.3847/1538-4365/abef67](https://doi.org/10.3847/1538-4365/abef67)
- Kehoe, E., Shapley, A. E., Förster Schreiber, N. M., et al. 2024, arXiv e-prints, arXiv:2406.07621, doi: [10.48550/arXiv.2406.07621](https://doi.org/10.48550/arXiv.2406.07621)
- Kluyver, T., Ragan-Kelley, B., Pérez, F., et al. 2016, in *IOS Press*, 87–90, doi: [10.3233/978-1-61499-649-1-87](https://doi.org/10.3233/978-1-61499-649-1-87)
- Kroupa, P. 2001, *MNRAS*, 322, 231, doi: [10.1046/j.1365-8711.2001.04022.x](https://doi.org/10.1046/j.1365-8711.2001.04022.x)
- Lamers, H. J. G. L. M., & Cassinelli, J. P. 1999, *Introduction to Stellar Winds*
- Leitherer, C., Ortiz Otálvaro, P. A., Bresolin, F., et al. 2010, *ApJS*, 189, 309, doi: [10.1088/0067-0049/189/2/309](https://doi.org/10.1088/0067-0049/189/2/309)
- Leitherer, C., Schaerer, D., Goldader, J. D., et al. 1999, *ApJS*, 123, 3, doi: [10.1086/313233](https://doi.org/10.1086/313233)
- Li, Z., Gronke, M., & Steidel, C. C. 2024, *MNRAS*, 529, 444, doi: [10.1093/mnras/stae469](https://doi.org/10.1093/mnras/stae469)

- Liu, G., Zakamska, N. L., Greene, J. E., Nesvadba, N. P. H., & Liu, X. 2013, *MNRAS*, 436, 2576, doi: [10.1093/mnras/stt1755](https://doi.org/10.1093/mnras/stt1755)
- Loaiza-Agudelo, M., Overzier, R. A., & Heckman, T. M. 2020, *ApJ*, 891, 19, doi: [10.3847/1538-4357/ab6f6b](https://doi.org/10.3847/1538-4357/ab6f6b)
- Marasco, A., Belfiore, F., Cresci, G., et al. 2023, *A&A*, 670, A92, doi: [10.1051/0004-6361/202244895](https://doi.org/10.1051/0004-6361/202244895)
- Markwardt, C. B. 2009, in *Astronomical Society of the Pacific Conference Series*, Vol. 411, *Astronomical Data Analysis Software and Systems XVIII*, ed. D. A. Bohlender, D. Durand, & P. Dowler, 251. <https://arxiv.org/abs/0902.2850>
- Martin, C. L. 2005, *ApJ*, 621, 227, doi: [10.1086/427277](https://doi.org/10.1086/427277)
- . 2006, *ApJ*, 647, 222, doi: [10.1086/504886](https://doi.org/10.1086/504886)
- Martin, C. L., Dijkstra, M., Henry, A., et al. 2015, *ApJ*, 803, 6, doi: [10.1088/0004-637X/803/1/6](https://doi.org/10.1088/0004-637X/803/1/6)
- Martín-Fernández, P., Jiménez-Vicente, J., Zurita, A., Mediavilla, E., & Castillo-Morales, Á. 2016, *MNRAS*, 461, 6, doi: [10.1093/mnras/stw1048](https://doi.org/10.1093/mnras/stw1048)
- Mingozzi, M., James, B. L., Arellano-Córdova, K. Z., et al. 2022, arXiv e-prints, arXiv:2209.09047. <https://arxiv.org/abs/2209.09047>
- Modigliani, A., Goldoni, P., Royer, F., et al. 2010, in *Society of Photo-Optical Instrumentation Engineers (SPIE) Conference Series*, Vol. 7737, *Observatory Operations: Strategies, Processes, and Systems III*, ed. D. R. Silva, A. B. Peck, & B. T. Soifer, 773728, doi: [10.1117/12.857211](https://doi.org/10.1117/12.857211)
- Naab, T., & Ostriker, J. P. 2017, *ARA&A*, 55, 59, doi: [10.1146/annurev-astro-081913-040019](https://doi.org/10.1146/annurev-astro-081913-040019)
- Newman, S. F., Shapiro Griffin, K., Genzel, R., et al. 2012a, *ApJ*, 752, 111, doi: [10.1088/0004-637X/752/2/111](https://doi.org/10.1088/0004-637X/752/2/111)
- Newman, S. F., Genzel, R., Förster-Schreiber, N. M., et al. 2012b, *ApJ*, 761, 43, doi: [10.1088/0004-637X/761/1/43](https://doi.org/10.1088/0004-637X/761/1/43)
- Osterbrock, D. E., & Ferland, G. J. 2006, *Astrophysics of gaseous nebulae and active galactic nuclei*
- Pan, H.-A., Lim, J., Matsushita, S., Wong, T., & Ryder, S. 2013, *ApJ*, 768, 57, doi: [10.1088/0004-637X/768/1/57](https://doi.org/10.1088/0004-637X/768/1/57)
- Perna, M., Arribas, S., Catalán-Torrecilla, C., et al. 2020, *A&A*, 643, A139, doi: [10.1051/0004-6361/202038328](https://doi.org/10.1051/0004-6361/202038328)
- Perrotta, S., George, E. R., Coil, A. L., et al. 2021, *ApJ*, 923, 275, doi: [10.3847/1538-4357/ac2fa4](https://doi.org/10.3847/1538-4357/ac2fa4)
- Perrotta, S., Coil, A. L., Rupke, D. S. N., et al. 2023, *ApJ*, 949, 9, doi: [10.3847/1538-4357/acc660](https://doi.org/10.3847/1538-4357/acc660)
- Prochaska, J. X., Wolfe, A. M., Howk, J. C., et al. 2007, *ApJS*, 171, 29, doi: [10.1086/513714](https://doi.org/10.1086/513714)
- Prusinski, N. Z., Erb, D. K., & Martin, C. L. 2021, *AJ*, 161, 212, doi: [10.3847/1538-3881/abe85b](https://doi.org/10.3847/1538-3881/abe85b)
- Reddy, N. A., Steidel, C. C., Pettini, M., & Bogosavljević, M. 2016, *ApJ*, 828, 107, doi: [10.3847/0004-637X/828/2/107](https://doi.org/10.3847/0004-637X/828/2/107)
- Reddy, N. A., Kriek, M., Shapley, A. E., et al. 2015, *ApJ*, 806, 259, doi: [10.1088/0004-637X/806/2/259](https://doi.org/10.1088/0004-637X/806/2/259)
- Reichardt Chu, B., Fisher, D. B., Chisholm, J., et al. 2024, arXiv e-prints, arXiv:2402.17830, doi: [10.48550/arXiv.2402.17830](https://doi.org/10.48550/arXiv.2402.17830)
- Rupke, D. S., Veilleux, S., & Sanders, D. B. 2002, *ApJ*, 570, 588, doi: [10.1086/339789](https://doi.org/10.1086/339789)
- Rupke, D. S. N., & Veilleux, S. 2013, *ApJ*, 768, 75, doi: [10.1088/0004-637X/768/1/75](https://doi.org/10.1088/0004-637X/768/1/75)
- Saldana-Lopez, A., Schaerer, D., Chisholm, J., et al. 2022, *A&A*, 663, A59, doi: [10.1051/0004-6361/202141864](https://doi.org/10.1051/0004-6361/202141864)
- Schlafly, E. F., & Finkbeiner, D. P. 2011, *ApJ*, 737, 103, doi: [10.1088/0004-637X/737/2/103](https://doi.org/10.1088/0004-637X/737/2/103)
- Scuderi, S., Bonanno, G., di Benedetto, R., Spadaro, D., & Panagia, N. 1992, *ApJ*, 392, 201, doi: [10.1086/171418](https://doi.org/10.1086/171418)
- Senchyna, P., Stark, D. P., Charlot, S., et al. 2021, *MNRAS*, 503, 6112, doi: [10.1093/mnras/stab884](https://doi.org/10.1093/mnras/stab884)
- Senchyna, P., Stark, D. P., Vidal-García, A., et al. 2017, *MNRAS*, 472, 2608, doi: [10.1093/mnras/stx2059](https://doi.org/10.1093/mnras/stx2059)
- Senchyna, P., Stark, D. P., Charlot, S., et al. 2022, *ApJ*, 930, 105, doi: [10.3847/1538-4357/ac5d38](https://doi.org/10.3847/1538-4357/ac5d38)
- Sheinis, A. I., Bolte, M., Epps, H. W., et al. 2002, *PASP*, 114, 851, doi: [10.1086/341706](https://doi.org/10.1086/341706)
- Sheth, K., Regan, M., Hinz, J. L., et al. 2010, *PASP*, 122, 1397, doi: [10.1086/657638](https://doi.org/10.1086/657638)
- Shopbell, P. L., & Bland-Hawthorn, J. 1998, *ApJ*, 493, 129, doi: [10.1086/305108](https://doi.org/10.1086/305108)
- Soto, K. T., & Martin, C. L. 2012, *ApJS*, 203, 3, doi: [10.1088/0067-0049/203/1/3](https://doi.org/10.1088/0067-0049/203/1/3)
- Steidel, C. C., Erb, D. K., Shapley, A. E., et al. 2010, *ApJ*, 717, 289, doi: [10.1088/0004-637X/717/1/289](https://doi.org/10.1088/0004-637X/717/1/289)
- Steidel, C. C., Rudie, G. C., Strom, A. L., et al. 2014, *ApJ*, 795, 165, doi: [10.1088/0004-637X/795/2/165](https://doi.org/10.1088/0004-637X/795/2/165)
- Strom, A. L., Steidel, C. C., Rudie, G. C., et al. 2017, *ApJ*, 836, 164, doi: [10.3847/1538-4357/836/2/164](https://doi.org/10.3847/1538-4357/836/2/164)
- Strom, A. L., Rudie, G. C., Trainor, R. F., et al. 2023, *ApJL*, 958, L11, doi: [10.3847/2041-8213/ad07dc](https://doi.org/10.3847/2041-8213/ad07dc)
- Sugahara, Y., Ouchi, M., Lin, L., et al. 2017, *ApJ*, 850, 51, doi: [10.3847/1538-4357/aa956d](https://doi.org/10.3847/1538-4357/aa956d)
- Swinbank, A. M., Harrison, C. M., Tiley, A. L., et al. 2019, *MNRAS*, 487, 381, doi: [10.1093/mnras/stz1275](https://doi.org/10.1093/mnras/stz1275)
- Thompson, T. A., & Heckman, T. M. 2024, arXiv e-prints, arXiv:2406.08561, doi: [10.48550/arXiv.2406.08561](https://doi.org/10.48550/arXiv.2406.08561)
- Urrutia, T., Wisotzki, L., Kerutt, J., et al. 2019, *A&A*, 624, A141, doi: [10.1051/0004-6361/201834656](https://doi.org/10.1051/0004-6361/201834656)
- Veilleux, S., Maiolino, R., Bolatto, A. D., & Aalto, S. 2020, *A&A Rv*, 28, 2, doi: [10.1007/s00159-019-0121-9](https://doi.org/10.1007/s00159-019-0121-9)

- Vernet, J., Dekker, H., D’Odorico, S., et al. 2011, *A&A*, 536, A105, doi: [10.1051/0004-6361/201117752](https://doi.org/10.1051/0004-6361/201117752)
- Weldon, A., Reddy, N. A., Coil, A. L., et al. 2024, arXiv e-prints, arXiv:2404.05725, doi: [10.48550/arXiv.2404.05725](https://doi.org/10.48550/arXiv.2404.05725)
- Whitaker, K. E., Franx, M., Leja, J., et al. 2014, *ApJ*, 795, 104, doi: [10.1088/0004-637X/795/2/104](https://doi.org/10.1088/0004-637X/795/2/104)
- Whittle, M. 1985, *MNRAS*, 213, 1, doi: [10.1093/mnras/213.1.1](https://doi.org/10.1093/mnras/213.1.1)
- Wood, C. M., Tremonti, C. A., Calzetti, D., et al. 2015, *MNRAS*, 452, 2712, doi: [10.1093/mnras/stv1471](https://doi.org/10.1093/mnras/stv1471)
- Xu, X., Arav, N., Miller, T., Kriss, G. A., & Plesha, R. 2020, *ApJS*, 247, 42, doi: [10.3847/1538-4365/ab5f68](https://doi.org/10.3847/1538-4365/ab5f68)
- Xu, X., Heckman, T., Yoshida, M., Henry, A., & Ohyama, Y. 2023a, *ApJ*, 956, 142, doi: [10.3847/1538-4357/acfa71](https://doi.org/10.3847/1538-4357/acfa71)
- Xu, X., Henry, A., Heckman, T., et al. 2022a, *ApJ*, 933, 202, doi: [10.3847/1538-4357/ac7225](https://doi.org/10.3847/1538-4357/ac7225)
- Xu, X., Heckman, T., Henry, A., et al. 2022b, *ApJ*, 933, 222, doi: [10.3847/1538-4357/ac6d56](https://doi.org/10.3847/1538-4357/ac6d56)
- . 2023b, arXiv e-prints, arXiv:2301.11498, doi: [10.48550/arXiv.2301.11498](https://doi.org/10.48550/arXiv.2301.11498)
- Xu, Y., Ouchi, M., Nakajima, K., et al. 2023c, arXiv e-prints, arXiv:2310.06614, doi: [10.48550/arXiv.2310.06614](https://doi.org/10.48550/arXiv.2310.06614)
- Zhang, Y., Ouchi, M., Nakajima, K., et al. 2024, *ApJ*, 970, 19, doi: [10.3847/1538-4357/ad47f4](https://doi.org/10.3847/1538-4357/ad47f4)